University of Connecticut
OpenCommons@UConn

Doctoral Dissertations

University of Connecticut Graduate School

4-29-2014

Optical and Photoacoustic Imaging for Ovarian Cancer Detection

Tianheng Wang
tiw09002@engr.uconn.edu

Follow this and additional works at: https://opencommons.uconn.edu/dissertations

Recommended Citation

Wang, Tianheng, "Optical and Photoacoustic Imaging for Ovarian Cancer Detection" (2014). *Doctoral Dissertations*. 357.
https://opencommons.uconn.edu/dissertations/357

Optical and Photoacoustic Imaging for Ovarian Cancer Detection

Tianheng Wang

University of Connecticut, 2014

Ovarian cancer is the fifth most common cancer among women and has the highest mortality rate of all gynecologic cancers. Current clinical imaging modalities are limited by poor sensitivity and specificity. Therefore, there is an urgent need to develop effective tools to detect ovarian cancer. In this dissertation, two imaging modalities, optical coherence tomography (OCT) and photoacoustic imaging have been investigated for ovarian cancer detection and characterization.

In the first modality, optical scattering coefficient, phase retardation and phase retardation rate were quantitatively extracted from polarization-sensitive OCT (PS-OCT) images. A highly positive correlation was found between those three parameters and collagen content, which is an indicator of ovarian tissue malignancy. Malignant ovarian tissue showed statistically significant lower scattering and birefringence property than normal ovarian tissue. A three-parameter logistic model was developed to diagnose ovaries as malignant or normal. The extracted parameters from 33 ovaries were used as input predictors to train the logistic model, and 10 additional ovaries were tested using this trained model. 100% sensitivity and specificity were achieved in the training group; 100% sensitivity and 83.3% specificity were achieved in the testing group. In the second modality, a laser pulse stretching scheme is designed to improve laser energy delivery in photoacoustic imaging in order to improve *in vivo* ovarian cancer detection based on optical fiber illumination. The effects of pulse width on photoacoustic detection using different ultrasound transducers were systematically investigated by simulations and experiments. In addition, an optical-resolution photoacoustic microscopy (PAM) was developed to map microvasculature networks in ovarian tissue. The feasibility of PAM to differentiate malignant from normal ovaries was explored by comparing PAM images morphologically. PAM images of both normal and malignant ovarian tissue match the histology. Based on the observed differences between PAM images of normal and malignant ovarian tissue in microvasculature features and distributions, seven parameters were quantitatively extracted and applied to a logistic model for ovarian tissue diagnosis. A specificity of 81.3% and a sensitivity of 88.2% were achieved. Those results have demonstrated the great potential of OCT and photoacoustic imaging for clinical ovarian cancer detection.

Optical and Photoacoustic Imaging for Ovarian Cancer Detection

Tianheng Wang

B.S., Harbin Institute of Technology, China, 2007

M.S., Harbin Institute of Technology, China, 2009

A Dissertation

Submitted in Partial Fulfillment of the

Requirements for the Degree of Doctor of Philosophy

at the

University of Connecticut

2014

Copyright by

Tianheng Wang

2014

APPROVAL PAGE

Doctor of Philosophy Dissertation

Optical and Photoacoustic Imaging for Ovarian Cancer Detection

Presented by

Tianheng Wang, B.S., M.S.

Major Advisor______________________________________

Quing Zhu

Associate Advisor______________________________________

Rajeev Bansal

Associate Advisor______________________________________

Molly Brewer

University of Connecticut

2014

Acknowledgements

It was a great honor to have the opportunity to join the Optical and Ultrasound Imaging Lab at UConn. I learned so much during my Ph.D. study and research. This work could not be accomplished without the help of many people.

First of all, I would like to express my deepest appreciation to my advisor Dr. Quing Zhu for her continuous encouragement, guidance and sincere caring. Her exceptional expertise in optical and ultrasound imaging expanded my knowledge scope and inspired me to make great progress. I also learned a lot from Dr. Zhu beyond knowledge. Her academic attitude, pursuit of innovation, persistence in research, and hardworking deeply impress and impact me. This dissertation could not be accomplished without Dr. Zhu's constant help and guidance.

I am so grateful to my associate advisors and committee members, Dr. Rajeev Bansal, Dr. Molly Brewer, Dr. Faquir Jain, and Dr. Helena Silva. Thanks for their suggestions and comments, and spending time reviewing this thesis. Special thanks to Dr. Brewer for providing imaging samples and medical knowledge. I also would like to acknowledge Xiaohong Wang and Dr. Melinda Sanders from UConn Health Center for the help on histopathology.

This work could not be done without the help from my labmates. I had great time working in this lab and would like to acknowledge all the team members, Dr. Yi Yang, Dr. Patrick Kumavor, Dr. Umar Alqasemi, Hai Li, Hassan Salehi, Sreyankar Nandy, Dr. Chen Xu, Dr. Yan Xu, Feifei Zhou, Dr. Nrusingh Biswal, Dr. Andres Aguirre, Dr. Saeid Zanganeh, Dr. Behnoosh Tavakoli, Guangqian Yuan, Yanping Gong, Hamed Vavadi,

Mohsen Erfanzadeh, Akaram Abuteen, Dr. Yueli Chen, Dr. Yasaman Ardeshirpour, Dr. Rui Wang, and Mohammed Zakaria.

I also would like to acknowledge our funding source from National Institute of Health and Donaghue Medical Research Foundation.

Finally, I would like to thank my family, especially my wife, my parents, and my sister. Thanks for continuously supporting and encouraging me to pursue my dreams.

Table of Contents

1 Introduction 1
  1.1 Ovarian cancer 1
  1.2 Optical and photoacoustic imaging 1
  1.3 Motivation of this work 3
  1.4 Organization of this dissertation 4
2 Principles of optical coherence tomography and photoacoustic imaging 7
  2.1 Optical coherence tomography 7
    2.1.1 Time-domain OCT 7
    2.1.2 Fourier-domain OCT 8
  2.2 Photoacoustic imaging 9
    2.2.1 Photoacoustic generation 9
    2.2.2 Photoacoustic propagation and detection 11
3 Quantitative analysis of optical scattering coefficient and phase retardation for ovarian tissue characterization [1,2] 13
  3.1 Introduction 13
  3.2 Materials and methods 14
    3.2.1 PS-OCT 14
    3.2.2 Optical scattering coefficient and phase retardation 16
    3.2.3 Ovary sample 18
    3.2.4 Histopathology and collagen area fraction 19
  3.3 Results and discussion 20
  3.4 Summary 28
4 A three-parameter logistic model for ovarian cancer detection using polarization-sensitive optical coherence tomography [1] 31
  4.1 Introduction 31
  4.2 Materials and methods 32
    4.2.1 Ovary sample and histopathology 32
    4.2.2 PS-OCT systems 32
    4.2.3 Phase retardation rate 34
    4.2.4 Optical scattering coefficient and phase retardation 35
    4.2.5 Logistic model and receiver operating characteristic curve 35
  4.3 Results and discussion 37
    4.3.1 Statistical results of 33 ovaries imaged by TD-PS-OCT 37
    4.3.2 Training results based on logistic model using the 33-ovary data 40
    4.3.3 Testing results of 10 ovaries imaged by FD-PS-OCT 41
  4.4 PS-OCT based on polarization-maintaining fiber 43
  4.5 Summary 45
5 Application of laser pulse stretching scheme for efficiently delivering laser energy in photoacoustic imaging [1] 47
  5.1 Introduction 47
  5.2 Methods 50
    5.2.1 Simulation method 50
    5.2.2 Ring-cavity pulse stretching system 51
    5.2.3 Experimental setup 53

        - 5.2.4 Imaging quality comparison 54
    - 5.3 Simulation and experimental results 55
        - 5.3.1 Simulations 55
        - 5.3.2 Experimental results 57
    - 5.4 Discussion and summary 68
- 6 Photoacoustic microscopy for ovarian cancer detection [1] 72
    - 6.1 Introduction 72
    - 6.2 Materials and methods 73
        - 6.2.1 Ovary sample 73
        - 6.2.2 PAM system 74
        - 6.2.3 Feature extraction 75
        - 6.2.4 Logistic model 76
    - 6.3 Results and discussion 77
        - 6.3.1 Lateral resolution test 77
        - 6.3.2 Ovarian tissue characterization 78
    - 6.4 Photoacoustic microscopy with a laser diode excitation 83
    - 6.5 Summary 85
- 7 Conclusions and future work 88
- **List of publications** 91

List of Tables

Table 3-1. Patient information and measurement results.. 22
Table 4-1. Summary of logistic model results by using different parameters. SC: scattering coefficient, PR: phase retardation, PRR: phase retardation rate, Th: threshold.. 41
Table 4-2. Summary of testing results by using the same threshold of the training group. SC: scattering coefficient, PR: phase retardation, PRR: phase retardation rate, Th: threshold. 42
Table 5-1. Photoacoustic image quality comparison using same energy of 17 ns and 37 ns pulses. Contrast (resolution) ratio = Contrast (resolution) obtained with 37 ns laser pulse / 17 ns laser pulse. (a) Music wire comparison. (b) Blood tube comparison. 67
Table 5-2. Photoacoustic image quality comparison using 17 ns and 1.5-fold energy of 37 ns pulses... 67

List of Figures

Figure 2-1. Typical time-domain OCT system configuration. 8
Figure 3-1. Time domain PS-OCT system configuration. P: polarizer; BS: beam splitter; PBS: polarization beam splitter. 16
Figure 3-2. Optical scattering coefficient and average phase retardation measurement example. (a) conventional OCT image; (b) fitting curves; (c) phase retardation image; (d) result table. White dashed rectangular: selected area for fitting; scale bar: 0.5 mm. 18
Figure 3-3. One set of examples from normal (a-c) and malignant (d-f) ovarian tissue. (a), (d): OCT images; (b), (e): H&E histology; (c), (f): picrosirius red stains; blue arrows: collagen bundles. 20
Figure 3-4. Conventional OCT (a, c) and phase retardation images (b, d) from normal (a, b) and malignant (c, d) ovarian tissue. Scale bar: 0.5 mm. 21
Figure 3-5. Histograms of estimated scattering coefficient (a), phase retardation (b) and collagen area fraction (c) for normal and malignant ovary groups. 23
Figure 3-6. Scatter plots of estimated scattering coefficient (a), phase retardation (b) and CAF (c) of each ovary for normal and malignant ovary groups. 25
Figure 3-7. Two-parameter (estimated optical scattering coefficient and average phase retardation) plot. 26
Figure 3-8. (a) Positive correlation demonstration between estimated scattering coefficient and collagen content; (b) Positive correlation demonstration between phase retardation and collagen content. The blue dashed lines show 95% prediction intervals. 27
Figure 4-1. TD/FD-PS-OCT systems configuration. P: polarizer; BS: beam splitter; PBS: polarization beam splitter; QWP: quarter-wave plate; M: mirror; PD: photodetector. 33
Figure 4-2. Example of calculating the phase retardation rate. (a) Phase retardation image; white dashed rectangular: selected area for fitting; scale bar: 0.5mm; (b) averaged A-lines and numerical fitting curves. 35
Figure 4-3. Box plots of normal and malignant ovary groups. (a) Optical scattering coefficient; (b) phase retardation; (c) phase retardation rate; (d) collagen area fraction. 38
Figure 4-4. (a) Scatter plot of phase retardation rate of normal and malignant ovary groups. (b) Positive correlation demonstration between phase retardation rate and collagen content; the blue dashed lines show 95% confidence interval. ... 39
Figure 4-5. ROC curves and AUC of different prediction models: training results. 40
Figure 4-6. ROC curves and AUC of different prediction models: testing results... 43
Figure 4-7. Fiber-based PS-OCT system configuration. PC: polarization controller; PM: polarization-maintaining; QWP: quarter waveplate; NDF: neutral density filter; PBS: polarization beam splitter. 44
Figure 4-8. Conventional OCT (a) and phase retardation image (b) of human ovarian tissue. Scale bar: 0.5 mm. 45
Figure 5-1. Schematic of laser pulse stretching system based on a triangular ring cavity. M: mirror, BS: beam splitter. 52

Figure 5-2. Experimental setup of photoacoustic imaging using stretched laser pulse. M: mirror, BS: beam splitter. 54
Figure 5-3. Frequency-domain photoacoustic signals obtained with 6 ns and 50 ns laser pulses. (a) 0.25 mm-diameter target, (b) 2 mm-diameter target. 56
Figure 5-4. Simulations of normalized photoacoustic signal and normalized fiber damage threshold versus laser pulse width. The photoacoustic signal was obtained with (a) 1.3 MHz transducer, (b) 3.5 MHz transducer, (c) 6 MHz transducer. 58
Figure 5-5. Profile of laser pulses. (a) Initial 17 ns laser pulse, (b) stretched 27 ns laser pulse, (c) stretched 37 ns laser pulse. 59
Figure 5-6. Simulations and experimental results of normalized photoacoustic signal and normalized fiber damage threshold versus laser pulse width. The photoacoustic signal was obtained with (a) 1.3 MHz transducer, (b) 3.5 MHz transducer, (c) 6 MHz transducer. 61
Figure 5-7. Photoacoustic images of 0.5 mm-diameter music wire obtained with (a) 1.3 MHz transducer, 17 ns laser pulse; (b) 1.3 MHz transducer, same energy of stretched 37 ns laser pulse. (c) 3.5 MHz transducer, 17 ns laser pulse; (d) 3.5 MHz transducer, same energy of stretched 37ns laser pulse. (e) 6 MHz transducer, 17ns laser pulse; (f) 6 MHz transducer, same energy of stretched 37ns laser pulse. 62
Figure 5-8. Photoacoustic images of blood tube obtained with (a) 1.3 MHz transducer, 17 ns laser pulse; (b) 1.3 MHz transducer, same energy of stretched 37 ns laser pulse. (c) 3.5 MHz transducer, 17 ns laser pulse; (d) 3.5 MHz transducer, same energy of stretched 37 ns laser pulse. (e) 6 MHz transducer, 17 ns laser pulse; (f) 6 MHz transducer, same energy of stretched 37n s laser pulse. 64
Figure 5-9. The beam line across the center of the target. (a) Illustration of contrast calculation. (b) Zoomed in of solid rectangular area in 5-9 (a) to illustrate resolution calculation. 65
Figure 5-10. Photoacoustic images of 0.5 mm-diameter music wire obtained with (a) 1.3 MHz transducer, 17 ns laser pulse; (b) 1.3 MHz transducer, 1.5-fold energy of stretched 37 ns laser pulse. (c) 3.5 MHz transducer, 17 ns laser pulse; (d) 3.5 MHz transducer, 1.5-fold energy of stretched 37 ns laser pulse. (e) 6 MHz transducer, 17 ns laser pulse; (f) 6 MHz transducer, 1.5-fold energy of stretched 37 ns laser pulse. 66
Figure 6-1. Configuration of the OR-PAM system. 74
Figure 6-2. (a) PAM MAP image of a 7 µm carbon fiber, scale bar: 50 µm; (b) normalized cross-sectional profile of the carbon fiber along the dotted line in (a). 77
Figure 6-3. PAM MAP image of a mouse ear. 78
Figure 6-4. PAM images of (a) normal ovarian tissue and (b) malignant ovarian tissue; (c) H&E corresponding to (a); (d) H&E corresponding to (b); scale bar: 300 µm; arrows: blood vessels. 79
Figure 6-5. (a) Mean Radon transform and Gaussian fitting of Figure 6-4 (a), fitting SD: 74, fitting error: 1.5; (b) mean Radon transform and Gaussian fitting of Figure 6-4 (b), fitting SD: 91, fitting error: 8.3. 80

Figure 6-6. Boxplots of (a) low frequency; (b) high frequency; (c) Gaussian fitting SD; (d) Gaussian fitting error; (e) statistical mean; (f) Gamma mean; (g) Gamma variance. 82
Figure 6-7. ROC curves of (a) training set; (b) testing set.. 82
Figure 6-8. Configuration of the laser-diode PAM system....................................... 83
Figure 6-9. Profile of the diode laser; the pulse width is 124 ns. 84
Figure 6-10. MAP image of black-thread mesh obtained by laser-diode PAM. 84

1 Introduction

1.1 Ovarian cancer

Ovarian cancer ranks fifth in cancer deaths and has the highest mortality rate among all the gynecologic cancers with the 5-year survival rate of 44%. There are approximately 21,980 estimated new cases of ovarian cancer in the United States in 2014 and an estimated 14,270 deaths [1]. The majority of ovarian cancer cases are diagnosed at Stage III and Stage IV due to unreliable early symptoms as well as poor screening techniques. There is no effective diagnostic tool for the early detection of ovarian cancer for those high risk women. Two landmark studies on prophylactic oophorectomy (PO) for women who carry BRCA 1 or BRCA 2 mutations were reported in 2002 [2,3]. PO reduces the risk of ovarian cancer by more than 50%, and has been accepted as the standard care for high risk women. However, there appears to be a higher mortality rate for premenopausal oophorectomy. These high risk women are not candidates for hormone replacement therapy due to their increased risk of breast cancer [4]. It has been found that PO increases the mortality of women undergoing oophorectomy before the age of 45 [4] or even before the age of 55 to 60 [5]. Therefore, there is an urgent need to develop effective tools to detect ovarian cancer, so that the mortality rate of ovarian cancer can be reduced and the quality of patients’ life can be improved.

1.2 Optical and photoacoustic imaging

Medical imaging has a long history started by the discovery of X-ray in 1895. The most common medical imaging modalities to date include X-ray imaging, nuclear imaging, ultrasound imaging, and magnetic resonance imaging (MRI). Those imaging modalities are well developed and play important roles in clinical applications. However, each modality has its limitations and drawbacks, including the biological hazards of ionizing radiation, limited resolution and contrast, high cost of operation and maintenance.

Optical imaging has emerged as a promising biomedical imaging modality and demonstrated great potential for medical applications. Optical imaging could provide high sensitivity to functional changes of biological tissues in terms of light scattering, absorption, and fluorescence. In addition, the use of non-ionizing radiation and inexpensive instruments provide additional advantages of optical imaging compared with other traditional imaging modalities. Optical coherence tomography (OCT) is an emerging high resolution and noninvasive imaging technique that can perform cellular level imaging [6-8]. It measures backscattered and back-reflected light waves from microstructural features within the examined tissues. OCT typically achieves a resolution of several microns and a penetration depth of several millimeters. OCT instrumentation has been developing rapidly since it was first demonstrated in 1991 [9], from free-space to fiber-based configurations, from time-domain to Fourier-domain systems, from intensity-based OCT to different types of functional OCT, including polarization-sensitive OCT (PS-OCT) [10,11], Doppler OCT [12-14] and spectroscopic OCT [15-17]. OCT has been used to image biological tissues in human body and demonstrated great potential for clinical applications [18-20], including the ophthalmology, dentistry, gastrointestinal (GI) tract, coronary blood vessels, colon, breast tissue, etc.

Photoacoustic imaging is a hybrid medical imaging modality [21,22] and has demonstrated potential to image animal or human organs, such as the skin tissue [23], breast tissue [24], brain tissue [25], and ovarian tissue [26]. In photoacoustic imaging, an ultrasound transducer is used to measure the acoustic waves generated from thermal expansion caused by short width laser pulse absorption of biological tissue. The light absorption distribution which directly relates to tumor angiogenesis can be reconstructed from the received acoustic signals. Photoacoustic microscopy (PAM) is photoacoustic imaging with high spatial resolution [27,28]. Optical-resolution PAM (OR-PAM) with micron-scale resolution, is capable of mapping microvasculature networks in biological tissue and resolving microvessels with much higher resolution than conventional photoacoustic images obtained with ultrasound array transducer.

1.3 Motivation of this work

Currently, there is no reliable modality for ovarian cancer detection. The tumor marker CA 125 screening yields a sensitivity of less than 50%; transvaginal ultrasound has only 3.1% positive predictive value; pelvic exams yields a low sensitivity of only 30%; computed tomography (CT) scan for ovarian cancer detection achieves a specificity of 85%, however, the sensitivity is only 45% [29-33]. The motivation of this work is to develop more sensitive tools to effectively diagnose ovarian cancer, so that the use of PO can be minimized, and the mortality rate of ovarian cancer can be reduced. In this dissertation, two basic imaging modalities are used to characterize ovarian tissue. The first method is OCT, and the other method is photoacoustic imaging. OCT measures the scattering properties of biological tissue, and as a complement, photoacoustic imaging measures the absorption of the tissue. For photoacoustic imaging, two approaches are investigated. The first one is based on transvaginal approach for non-invasive detection. The other approach is PAM, which is capable of imaging microvasculature networks of ovarian tissue. OCT and PAM through fiber catheter and needle are promising for *in vivo* ovarian tissue imaging during the minimally invasive surgery.

1.4 Organization of this dissertation

This dissertation is organized into seven chapters. Chapter 1 introduces the background of ovarian cancer and some biomedical imaging methods. Chapter 2 provides the basic principles of the imaging modalities utilized in this dissertation, including OCT and photoacoustic imaging. Chapter 3 describes quantitative analysis of optical scattering coefficient and phase retardation properties of ovarian tissue based on PS-OCT. In chapter 4, an extended study of ovarian cancer characterization using a three-parameter logistic prediction model is described. In chapter 5, a laser pulse stretching scheme is studied for efficiently delivering laser energy in fiber-based photoacoustic imaging. Chapter 6 demonstrates the ability of PAM to map blood vessels in ovarian tissue, and describes the quantitative analysis of PAM images for ovarian tissue characterization. Finally, chapter 7 summarizes this dissertation.

References

1. Cancer Facts and Figures 2014. American Cancer Society 2014.
2. N. D. Kauff, J. M. Satagopan, M. E. Robson, L. Scheuer, M. Hensley, C. A. Hudis, N. A. Ellis, J. Boyd, P. I. Borgen, R. R. Barakat, L. Norton, M. Castiel, K. Nafa, and

K. Offit, “Risk-reducing salpingo-oophorectomy in women with a BRCA1 or BRCA2 mutation,” N. Engl. J. Med. 346(21), 1609-1615 (2002).

3. T. R. Rebbeck, H. T. Lynch, S. L. Neuhausen, S. A. Narod, L. Van't Veer, J. E. Garber, G. Evans, C. Isaacs, M. B. Daly, E. Matloff, O. I. Olopade, and B. L. Weber, “Prophylactic oophorectomy in carriers of BRCA1 or BRCA2 mutations,” N. Engl. J. Med. 346(21), 1616-1622 (2002).
4. W. A. Rocca, B. R. Grossardt, M. de Andrade, G. D. Malkasian, and L. J. Melton, “Survival patterns after oophorectomy in premenopausal women: a population-based cohort study,” Lancet Oncol. 7(10), 821-828 (2006).
5. J. S. Berek, E. Chalas, M. Edelson, D. H. Moore, W. M. Burke, W. A. Cliby, and A. Berchuck, “Prophylactic and risk-reducing bilateral salpingo-oophorectomy: recommendations based on risk of ovarian cancer,” Obstet. Gynecol. 116(3), 733-743 (2010).
6. J. G. Fujimoto, “Optical coherence tomography for ultrahigh resolution in vivo imaging,” Nat. Biotechnol. 21 11) 1361-1367, (2003).
7. A. F. Fercher, W. Drexler, C. K. Hitzenberger, and T. Lasser, “Optical coherence tomography-principles and applications,” Rep. Prog. Phys. 66(2), 239-303 (2003).
8. P. H. Tomlins and R. K. Wang, “Theory, developments and applications of optical coherence tomography,” J. Phys. D: Appl. Phys. 38(15), 2519-2535 (2005).
9. D. Huang D, E. A. Swanson, C. P. Lin, J. S. Schuman, W. G. Stinson, W. Chang, M. R. Hee, T. Flotte, K. Gregory, C. A. Puliafito, and J. G. Fujimoto JG, “Optical coherence tomography,” Science 254, 1178-1181 (1991).
10. M. R. Hee, D. Huang, E. A. Swanson, and J. G. Fujimoto, “Polarization-sensitive low-coherence reflectometer for birefringence characterization and ranging,” J. Opt. Soc. Am. B 9(6), 903-908 (1992).
11. J. F. de Boer and T. E. Milner, “Review of polarization sensitive optical coherence tomography and Stokes vector determination,” J. Biomed. Opt. 7(3) 359-371, (2002).
12. Z. Chen, Y. Zhao, S. M. Srinivas, J. S. Nelson, N. Prakash, R. D. Frostig, “Optical Doppler Tomography,” IEEE J. Sel. Top. Quantum Electron. 5(4), 1134-1142, (1999).
13. A. M. Rollins, S. Yazdanfar, J. K. Barton, and J. A. Izatt, “Real-time in vivo color Doppler optical coherence tomography,” J. Biomed. Opt. 7(1), 123-129 (2002).
14. D. Piao, L. Otis, and Q. Zhu, “Doppler angle and flow velocity mapping by combining Doppler shift and Doppler bandwidth measurements in optical Doppler tomography,” Opt. Lett. 28(13), 1120-1123 (2003).
15. J. M. Schmitt, S. H. Xiang, and K. M. Yung, “Differential absorption imaging with optical coherence tomography,” J. Opt. Soc. Am. A 15(9), 2288-2296 (1998).
16. U. Morgner, W. Drexler, F. X. Kärtner, X. D. Li, C. Pitris, E. P. Ippen, and J. G. Fujimoto, “Spectroscopic optical coherence tomography,” Opt. Lett. 25(2), 111-113 (2000).
17. C. Xu, P. Carney, and S. Boppart, “Wavelength-dependent scattering in spectroscopic optical coherence tomography, Opt. Express 13(14), 5450-5462 (2005).
18. J. G. Fujimoto, C. Pitris, B. A. Boppart, and M. E. Brezinski, “Optical coherence tomography: an emerging technology for biomedical imaging and optical biopsy,” Neoplasia 2(1-2), 9-25 (2000).

19. B. J. Vakoc, D. Fukumura, R. K. Jain, and B. E. Bouma, “Cancer imaging by optical coherence tomography: preclinical progress and clinical potential,” Nat. Rev. Cancer 12(5), 363-368 (2012).
20. A. Karanasos, J. Ligthart, K. Witberg, G. van Soest, N. Bruining, and E. Regar, “Optical coherence tomography: potential clinical applications,” Curr. Cardiovasc. Imaging Rep. 5(4), 206-220 (2012).
21. M. H. Xu and L. H. V. Wang, “Photoacoustic imaging in biomedicine,” Rev. Sci. Instrum. 77(4), 041101 (2006).
22. C. H. Li and L. H. V. Wang, “Photoacoustic tomography and sensing in biomedicine,” Phys. Med. Biol. 54(19), R59-R97 (2009).
23. R. J. Zemp, R. Bitton, M. L. Li, K. K. Shung, G. Stoica, and L. V. Wang, “Photoacoustic imaging of the microvasculature with a high-frequency ultrasound array transducer,” J. Biomed. Opt. 12(1), 010501 (2007).
24. S. Manohar, A. Kharine, J. C. van Hespen, W. Steenbergen, and T. G. van Leeuwen, “The twente photoacoustic mammoscope: system overview and performance,” Phys. Med. Biol. 50(11), 2543-2557 (2005).
25. E. Zhang, J. Laufer, and P. Beard, “Three-dimensional photoacoustic imaging of vascular anatomy in small animals using an optical detection system,” Proc. SPIE 6437, 64370S (2007).
26. A. Aguirre, P. Y. Guo, J. Gamelin, S. H. Yan, M. M. Sanders, M. Brewer, and Q. Zhu, "Coregistered three-dimensional ultrasound and photoacoustic imaging system for ovarian tissue characterization,” J. Biomed. Opt. 14(5), 054014 (2009).
27. L. V. Wang and S. Hu, “Photoacoustic tomography: in vivo imaging from organelles to organs,” Science 335, 1458-1462 (2012).
28. J. Yao and L. V. Wang, “Photoacoustic microscopy,” Laser Photon Rev. 7(5), 758-778 (2013).
29. J. Tammela and S. Lele, “New modalities in detection of recurrent ovarian cancer,” Curr. Opin. Obstet. Gynecol. 16(1), 5-9 (2004).
30. V. Nossov, M. Amneus, F. Su, J. Liang, J. M. T. Janco, S. T. Reddy, and R. Farias-Eisner, “The early detection of ovarian cancer: from traditional methods to proteomics. Can we really do better than serum CA-125,” Am. J. Obstet. Gynecol. 199(3), 215-223 (2008).
31. B. Van Calster, D. Timmerman, T. Bourne, A. C. Testa, C. Van Holsbeke, E. Domali, D. Jurkovic, P. Neven, S. Van Huffel, L. Valentin, “Discrimination between benign and malignant adnexal masses by specialist ultrasound examination versus serum CA-125,” J. Natl. Cancer Inst. 99(22), 1706-1714 (2007).
32. M. Goozner, “Personalizing ovarian cancer screening,” J. Natl. Cancer. Inst. 102(15), 1112-1113 (2010).
33. A. Shaaban and M. Rezvani, “Ovarian cancer: detection and radiologic staging,” Clin. Obstet. Gynecol. 52(1), 73-93 (2009).

2 Principles of optical coherence tomography and photoacoustic imaging

2.1 Optical coherence tomography

2.1.1 Time-domain OCT

OCT is analogous to B-mode ultrasound imaging, except that OCT uses light instead of sound. Figure 2-1 is a typical time-domain OCT (TD-OCT) system configuration. It consists of a Michelson interferometer with a low coherence light source. The low coherence light is split into reference and sample arm by a beam splitter, and the back-reflected light from sample and reference mirror is recombined at the beam splitter. If the difference of optical path length between reference and sample arm is within the coherence length of light source, the recombined beam can generate interference signals, which can be detected by the photodetector. The scattering information from sample at different depths can be obtained by scanning the reference mirror. B-scan image can be obtained by scanning the light beam or moving the sample. By performing two-dimensional spatial scanning, 3D image of the sample could be reconstructed. The axial resolution is defined by [1,2]:

$$\delta_z = l_c = \frac{2\ln 2}{\pi} \cdot \frac{\lambda_0^2}{\Delta\lambda} \tag{2-1}$$

where l_c is the coherence length, λ_0 and $\Delta\lambda$ are the central wavelength and bandwidth of the light source, respectively. The lateral resolution achieved by OCT is determined by the size of the focused beam:

$$\delta_x = \frac{4\lambda}{\pi} \cdot \frac{f}{d} \tag{2-2}$$

where *f* is the focal length of the objective lens, *d* is the spot size on the objective lens.

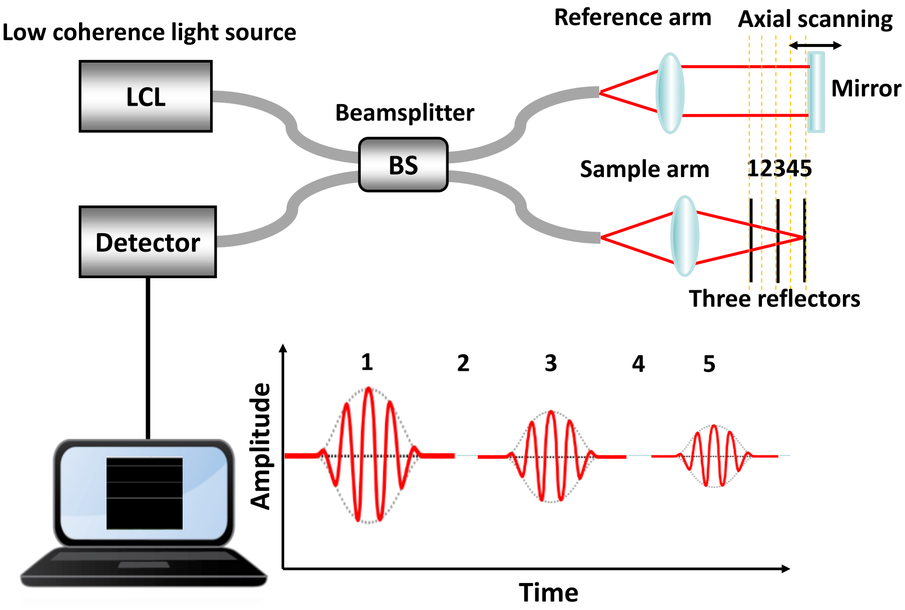
Low coherence light source
LCL
Detector
Beamsplitter
BS
Reference arm
Axial scanning
Mirror
Sample arm
12345
Three reflectors
Amplitude
Time
1
2
3
4
5

Figure 2-1. Typical time-domain OCT system configuration.

2.1.2 Fourier-domain OCT

The system described in 2.1.1 is a typical time-domain OCT setup. Fourier-domain OCT (FD-OCT) has demonstrated higher sensitivity and data acquisition speed compared with TD-OCT [3]. In FD-OCT, only lateral scan is needed. The depth information can be obtained from the Fourier transform of the detected frequency spectrum $I(\omega)$ to the time domain interference pattern $I(t)$ [2]:

$$I(t) = FT\{I(\omega)\} \tag{2-3}$$

where *FT* represents the Fourier transform operation. The interference pattern can be displayed either as a function of optical time of flight or equivalent TD-OCT reference mirror displacement.

FD-OCT can be implemented either as spectral-domain OCT (SD-OCT) or swept-source OCT (SS-OCT). In SD-OCT, a broadband light source and a dispersive spectrometer are applied to measure the interference pattern as a function of wavelength. In SS-OCT, a tunable laser source and a single detector are applied to detect the intensity by sweeping the source spectrum. Since no moving parts are required to obtain axial scans, FD-OCT significantly increases the data-acquisition speed.

2.2 Photoacoustic imaging

The discovery of the photoacoustic effect dates to 1880 when Alexander Graham Bell showed that thin discs emitted sound when it was exposed to a beam of sunlight that was rapidly interrupted with a rotating slotted disk [4,5]. Photoacoustic technique is amenable for biomedical applications. In photoacoustic imaging, only nonionizing radiation is used, it will not change properties of the biological tissue and is ideal for *in vivo* applications. In addition, the relationships between PA signals and the physical parameters of biological tissues are well defined, which permits the quantification of various physiological parameters.

2.2.1 Photoacoustic generation

The photoacoustic effect is a conversion between pulsed light and sound waves due to light absorption and localized thermal excitation. An object with light pulses illumination absorbs light energy, the absorbed energy converts into heat and causes temperature rise. The temperature rise results in thermal expansion, and generates acoustic waves due to pressure variation in the surrounding medium. The pressure rise is propagated as ultrasound waves, which is detected by ultrasound transducer.

Electromagnetic (EM) waves interact with charged particles by elastic scattering, Raman scattering, and absorption. In an absorption interaction, the absorbed energy can be transformed into heat or consumed in a chemical reaction, and can also be re-emitted as fluorescence. Only the portion which is turned into heat leads to the photoacoustic effect. In most cases of diagnostic photoacoustic detection, the heating effect dominates the absorption interaction. The absorption ability depends on the EM wavelength, EM polarization, molecular constitution, ion density, and environmental conditions.

The EM pulse used to generate photoacoustic pressure wave usually has a pulse width τ . τ should be short enough so that thermal diffusion can be neglected. This condition is called the thermal confinement condition [6]:

$$\tau < \tau_{th} = \frac{d_c^2}{4D_T} \tag{2-4}$$

where τ_{th} is the thermal confinement threshold, d_c is the characteristic dimension, and D_T is the thermal diffusivity. Under this condition, photoacoustic pressure generated in an acoustically homogenous and non-viscous medium is described by the function [7]:

$$\nabla^2 p(\vec{r},t) - \frac{1}{v_s^2}\frac{\partial^2}{\partial t^2} p(\vec{r},t) = -\frac{\beta}{C_p}\frac{\partial}{\partial t} H(\vec{r},t) \tag{2-5}$$

where $H(\vec{r},t)$ is a heating function defined as the thermal energy converted at spatial position $\vec{r}$ and time t by the EM radiation per unit volume per unit time; it is related to the specific optical power deposition and the optical fluence rate. C_p is the isobaric specific heat, β is the isobaric volume expansion coefficient and v_s is the acoustic speed. A sound or stress wave is produced because of the thermo-elastic expansion that is induced by a slight temperature rise, as a result of the energy deposition inside the biological tissue through the absorption of the incident EM energy. The excited photoacoustic signal is locally determined by the EM absorption and scattering properties, the thermal properties, including the thermal diffusivity and thermal expansion coefficient, and the elastic properties of the sample.

2.2.2 Photoacoustic propagation and detection

EM pulse excited pressure acts as an acoustic source and initiates further acoustic wave propagation in three-dimensional space. In the low-megahertz frequency range, ultrasound in soft tissues has the properties of low scattering and deep penetration [4,5]. The total attenuation results from the combined losses due to both absorption and scattering. The attenuation of all tissues is dependent on the temperature and frequency. Both ultrasound attenuation and EM absorption affect the photoacoustic detection depth. For optical waves, the propagation is usually modeled by the radiative transfer equation, involving the scattering coefficient μ_s, the absorption coefficient μ_a and phase function. The reduced scattering coefficient $\mu_s^{'}$ is also a very important parameter. Although the radiative transfer equation generally does not have exact analytical solutions, it can be solved by Monte Carlo simulations, or under the diffusion approximation. The absorption by the tissue plays an important role for the variations in the illumination depth, and consequently the detection depth of photoacoustic detection.

The ultrasound signal from the initial source reaches the tissue surface and then can be received by an ultrasound transducer. Different types of ultrasound transducers can be used, including single-element transducers, array transducers, integrated transducers and virtual point transducers. The most often used ultrasound detectors are based on piezoelectric materials, which have low thermal noise and high sensitivity and can provide a wide band of up to 100 MHz [4,5]. In addition to acoustic detection, the optical detection is also feasible. Optical methods are often based on photoacoustic-pressured-induced surface displacement or refraction index changes, and they have potential for non-contact measurement and rapid monitoring of large areas [8]. The disadvantages of optical detection relative to piezoelectric detection include lower sensitivity and higher noise.

References

1. A. F. Fercher, W. Drexler, C. K. Hitzenberger, and T. Lasser, "Optical coherence tomography-principles and applications," Rep. Prog. Phys. 66(2), 239-303 (2003).
2. P. H. Tomlins and R. K. Wang, "Theory, developments and applications of optical coherence tomography," J. Phys. D: Appl. Phys. 38(15), 2519-2535 (2005).
3. R. Leitgeb, C. K. Hitzenberger, and A. F. Fercher, "Performance of fourier domain vs. time domain optical coherence tomography," Opt Express 11(8), 889-894 (2003).
4. M. H. Xu and L. H. V. Wang, "Photoacoustic imaging in biomedicine," Rev. Sci. Instrum. 77(4), 041101 (2006).
5. C. H. Li and L. H. V. Wang, "Photoacoustic tomography and sensing in biomedicine," Phys. Med. Biol. 54(19), R59-R97 (2009).
6. X. D. Wang, D. L. Chamberland, and G. H. Xi, "Noninvasive reflection mode photoacoustic imaging through infant skull toward imaging of neonatal brains," J. Neurosci. Methods. 168(2), 412-421 (2008).
7. G. J. Diebold, T. Sun, and M. I. Khan, "Photoacoustic monopole radiation in one, two and three dimensions," Phys. Rev. Lett. 67(24), 3384-3387 (1991).
8. J. J. Niederhauser, D. Frauchiger, H. P. Weber, and M. Frenz, "Real-time optoacoustic imaging using a Schlieren transducer," Appl. Phys. Lett. 81(4), 571-573 (2002).

3 Quantitative analysis of optical scattering coefficient and phase retardation for ovarian tissue characterization [1,2]

3.1 Introduction

Optical coherence tomography (OCT) [3-7] measures backscattered light generated from an infrared light source directed to the tissues being examined. The morphological features of pre-neoplastic or early neoplastic changes have prompted the development of OCT for early-stage ovarian cancer detection [8-13]. OCT is sensitive to the changes in collagen which are typically seen as malignancy develops [12,13]. Polarization-sensitive OCT (PS-OCT) is a functional extension of conventional OCT and offers additional physiological information by measuring the polarization properties of biological tissues [14,15]. PS-OCT provides enhanced image contrast by making use of relative phase change of two orthogonal polarization detection channels. PS-OCT has been reported as an effective tool to detect and analyze fibrous tissues, including retinal nerve fiber layer [16,17], collagen fibers in skin [18-20], collagen and smooth muscle cell content in atherosclerotic plaques [21,22], and carious lesions [23, 24]. M. C. Pierce et al. [18] quantified the birefringence loss due to thermal denaturation of collagen, with mean phase retardation rate of 0.249 degree/µm measured from 26 burned skin sites, compared with that of 0.401 degree/µm from 26 normal skin sites. J. Strasswimmer et al. [19] indicated that PS-OCT can distinguish normal skin from tumor, and the tumor showed very little birefringence property, with the phase retardation rate much smaller than that of normal skin. S. K.

Nadkarni et al. [21] demonstrated that PS-OCT was capable of measuring the birefringence in plaques and in fibrous caps of necrotic core fibroatheroma after examining 87 aortic plaques obtained from 20 human cadavers. W. Kuo et al. [22] demonstrated that PS-OCT enabled differentiation of the atherosclerotic structures from normal tissue, and the quantified phase retardation results indicated that birefringence changes in fibrous and calcified plaques were more apparent than in normal vessels.

In this chapter, we report, to the best of our knowledge, the first study that uses PS-OCT for ovarian tissue characterization. A total of 33 *ex vivo* ovaries obtained from 18 patients were evaluated. We also measured the optical scattering properties of these ovaries from conventional OCT images and evaluated the potential of using two parameters of phase retardation and scattering property to quantitatively characterize normal and malignant ovarian tissues. The optical scattering coefficient and phase retardation from normal and malignant ovaries were extracted from conventional OCT and phase retardation images, respectively. The correlation between collagen content, as assessed from Sirius Red staining, estimated scattering coefficient and phase retardation properties were also investigated. Results demonstrate that scattering coefficient and phase retardation obtained from PS-OCT are potentially valuable parameters in differentiating normal from malignant ovaries.

3.2 Materials and methods

3.2.1 PS-OCT

Figure 3-1 depicts the time-domain PS-OCT system configuration. The key system features are briefly summarized here. The PS-OCT system consists of a 40 nm bandwidth super luminescent diode source (SLED) at center wavelength of 1310 nm and a Michelson interferometer. The 2 mW output light beam from the SLED passes a vertical polarizer and is evenly separated into sample arm and reference arm by a beam splitter (BS). In the sample arm, a quarter-waveplate QWP1 with the fast axis oriented at 45 degrees with respect to the horizontal direction is used to convert the linearly polarized light into the circularly polarized light. The circularly polarized light is focused by an objective lens to illuminate the examined sample. In the reference arm, another quarter-waveplate QWP2 with the fast axis oriented at 22.5 degrees with respect to the horizontal direction is placed right after the BS. After light beam back-propagating through the QWP2, the polarization state is changed to 45 degrees with respect to the horizontal direction which provides equal reference power for both orthogonal polarization channels. The reference mirror is driven by a stepper motor back and forth to provide 3.6 mm free space scanning depth. The back-scattered sample arm beam and the back-reflected reference arm beam recombine and form interferogram at the BS. The recombined light is separated by a polarization beam splitter (PBS) into horizontal and vertical components which are independently directed toward two identical photodetectors (D1 and D2). Conventional OCT is obtained by calculating the summation of the squares of both orthogonal polarization channel signals. Phase retardation image is obtained from measuring the arctangent between vertical and horizontal components.

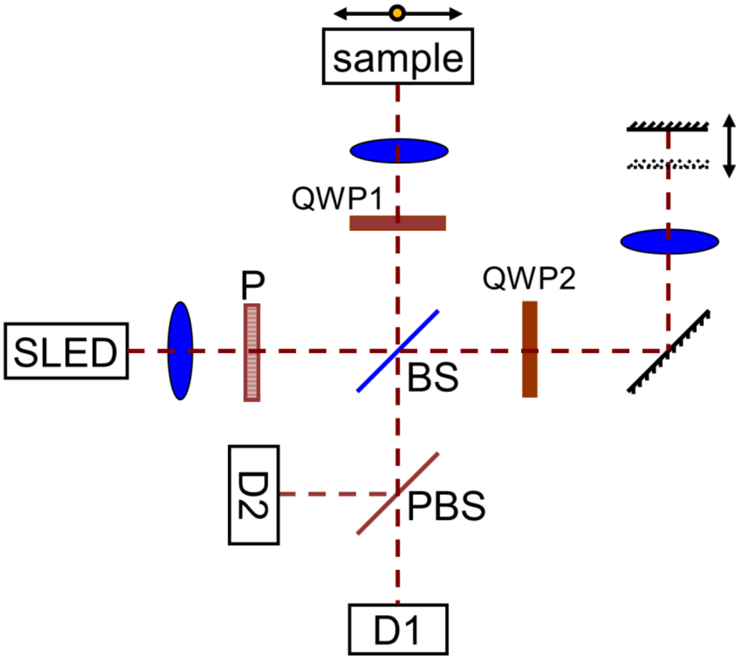

Figure 3-1. Time domain PS-OCT system configuration. P: polarizer; BS: beam splitter; PBS: polarization beam splitter.

3.2.2 Optical scattering coefficient and phase retardation

During imaging, similar conditions for all ovarian samples were achieved by mounting the ovary on a three-dimensional stage and adjusting tissue surface to the same depth position. The calculated numerical aperture 0.02 of the sample arm optics in our fixed focusing PS-OCT system was very low, which ensured the superficial scanning depth within the focal zone. Optical scattering coefficient was estimated by fitting compounded conventional OCT signal to a single scattering model based on Beer's law. Total attenuation coefficient μ_t is the summation of absorption coefficient (μ_a) and scattering coefficient (μ_s). As μ_a is much smaller than μ_s, μ_s is approximately equal to μ_t and it is a good estimate of the local scattering properties. Therefore, the quantitative μ_s extracted from OCT A-lines could reflect the local collagen content. In the single scattering model, the OCT signal is given by Beer’s law $I(z) = I_0\sqrt{\exp(-2\mu_s z)}$. The OCT signal $I(z)$ refers to the amplitude of the interference signal, the factor 2 accounts for the round trip attenuation and the square-root accounts for the fact that OCT measures the light amplitude instead of the intensity. In this study, 1 mm tissue corresponding to 74 A-lines was selected for averaging to minimize the speckle noise effect. A fitting example from a normal ovary is shown in Figure 3-2 where 3-2 (a) is a conventional OCT image and 3-2 (b) shows the fitting curves. The white dashed rectangular in Figure 3-2 (a) represents the selected 1mm area for fitting. The depth profile of one single A-line in the selected area is plotted as the black dashed curve and the compounded depth profile is shown as the blue solid curve in Figure 3-2 (b). The scattering coefficient was estimated by numerically fitting the compounded depth profile to the single scattering model shown as the red dotted curve in Figure 3-2 (b) and the value of 2.69 mm^{-1} is shown in Figure 3-2 (d). The phase retardation image is shown in Figure 3-2 (c). The dark blue represents phase retardation value of zero degree and the dark red shows phase retardation at 90 degrees. The average phase retardation of the same area marked by the selected white dashed rectangular in Figure 3-2 (c) was calculated and the value of 27.9 degrees is shown in Figure 3-2 (d) as well.

To calculate the specificity and sensitivity, thresholds of estimated scattering coefficient and phase retardation were selected, respectively. The specificity and sensitivity of each method were calculated as: specificity = TN / (TN + FP) × 100%; sensitivity = TP / (TP + FN) × 100%, where TP represents the number of true-positive findings, TN represents the number of true-negative findings, FP represents the number of false-positive findings, and FN represents the number of false-negative findings.

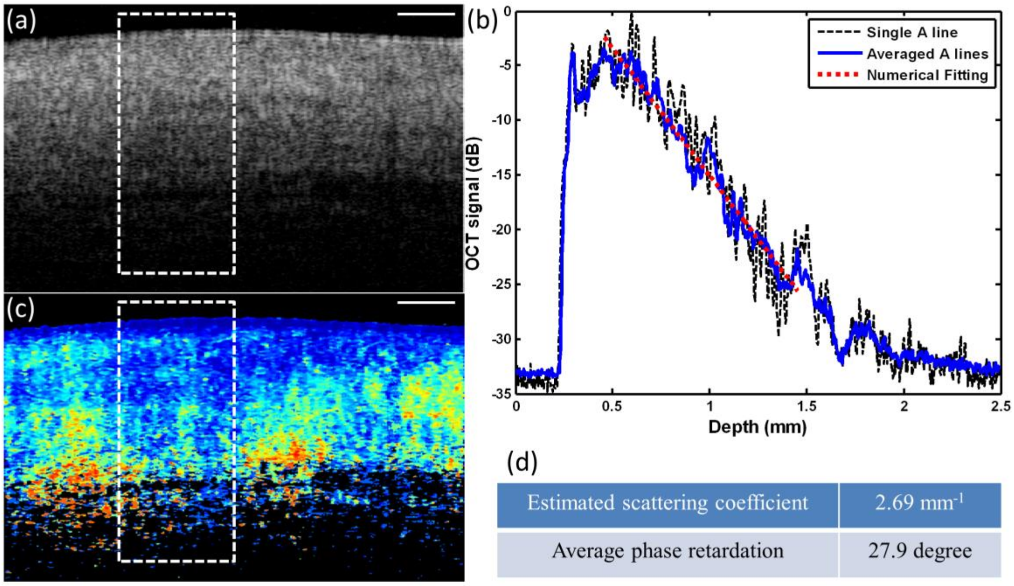

Estimated scattering coefficient	2.69 mm^{-1}
Average phase retardation	27.9 degree

Figure 3-2. Optical scattering coefficient and average phase retardation measurement example. (a) conventional OCT image; (b) fitting curves; (c) phase retardation image; (d) result table. White dashed rectangular: selected area for fitting; scale bar: 0.5 mm.

3.2.3 Ovary sample

In this study, 33 ovaries obtained from 18 patients whose age ranged from 37 to 78 (mean 61) were investigated using the PS-OCT system. Ovaries were extracted from patients undergoing PO at the University of Connecticut Health Center (UCHC). The patients were at risk for ovarian cancer or they had an ovarian mass suggestive of malignancy. This study was approved by the Institutional Review Boards of UCHC, and informed consent was obtained from all patients. Ovaries were kept in the 0.9% wt/vol NaCl solution and imaged within 24 hours after oophorectomy. After PS-OCT imaging, the ovaries were fixed in 10% formalin solution and returned to the Pathology Department for histological processing.

3.2.4 Histopathology and collagen area fraction

For histological evaluation, the ovaries were cut in 5 mm blocks parallel to the imaging plane, dehydrated with graded alcohol, embedded in paraffin and sectioned to 7 μm thickness using a paraffin microtome. Once the slides that correspond to the imaged planes were identified, they were stained using hematoxylin and eosin (H&E) for diagnosis. In addition, in order to analyze the collagen content, adjacent cross-section (7 μm apart from H&E cross-section) was sliced and Sirius Red staining protocol which specifically binds to collagen was applied to these slides. The digital image of histological ovarian surface tissue covering about 1 mm depth was acquired using a bright field microscope. The collagen content was quantitatively calculated using ImageJ software (National Institute of Health). The collagen area fraction (CAF) was measured as "Stained collagen area / tissue area". Figure 3-3 shows one set of examples from normal [Figure 3-3 (a)-(c)] and malignant [Figure 3-3 (d)-(f)] ovarian tissue imaged by OCT. The μ_s extracted from the OCT fitting areas marked as the white dashed region in Figure 3-3 (a) and 3-3 (d) are 2.86 mm^{-1} and 1.29 mm^{-1}, respectively. The stained red area in Figure 3-3 (c) and 3-3 (f) represents the collagen content. The collagen amount, structure, and arrangement are quite different between normal and malignant ovarian tissues. The normal ovary exhibits almost exclusively collagen with interspersed stromal cells and the collagen fibril is randomly oriented and wavy interlaced. The malignant ovary has less collagen content with collagen fibers unidirectionally organized into thicker bundles. A larger amount of collagen is found in normal ovarian tissue (CAF = 58.3%) than in malignant tissue (CAF = 8.4%).

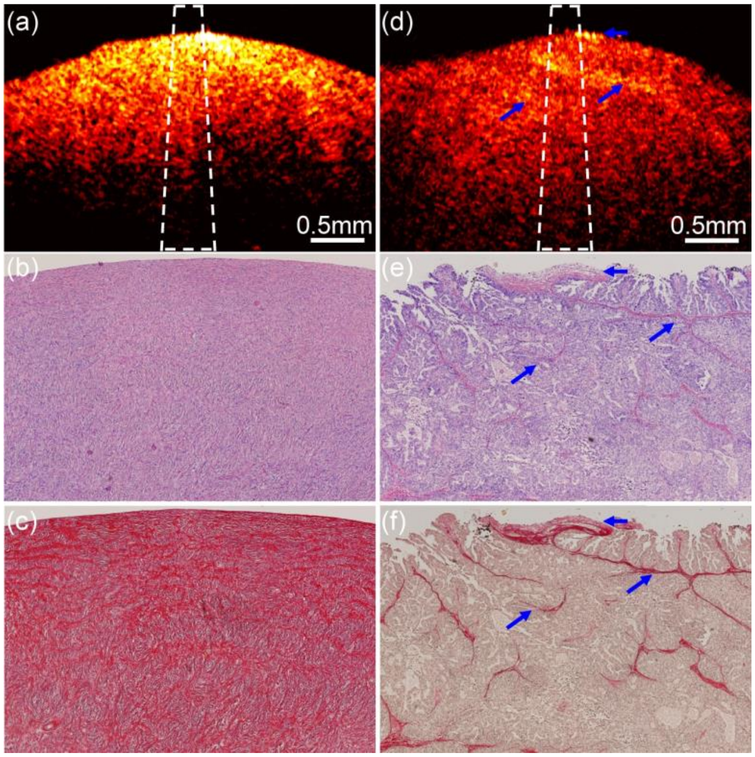

Figure 3-3. One set of examples from normal (a-c) and malignant (d-f) ovarian tissue. (a), (d): OCT images; (b), (e): H&E histology; (c), (f): picrosirius red stains; blue arrows: collagen bundles.

3.3 Results and discussion

Figure 3-4 shows one comparison example between normal [Figure 3-4 (a)-(b)] and malignant [Figure 3-4 (c)-(d)] ovarian tissue. Figure 3-4 (a) and 3-4 (c) are conventional OCT images while 3-4 (b) and 3-4 (d) are phase retardation images. The mean values of estimated scattering coefficients for Figure 3-4 (a) and 3-4 (c) are 3.07 mm^{-1} and 0.85 mm^{-1}, respectively. The mean values of phase retardation for Figure 3-4 (b) and 3-4 (d) are 30.0 and 12.9 degrees, respectively.

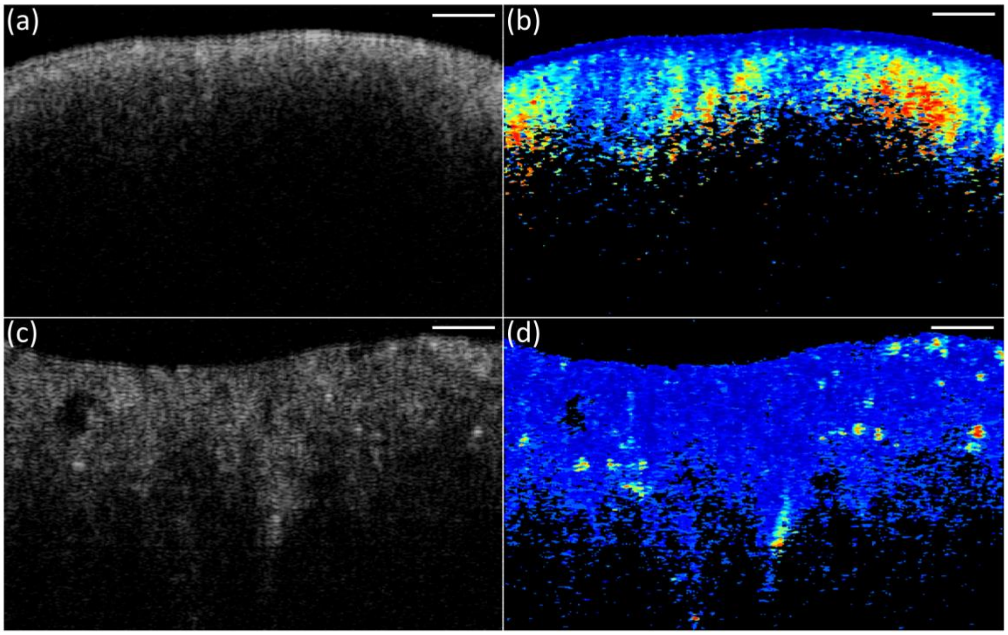

Figure 3-4. Conventional OCT (a, c) and phase retardation images (b, d) from normal (a, b) and malignant (c, d) ovarian tissue. Scale bar: 0.5 mm.

A total of 18 patients and 33 ovaries were imaged using the PS-OCT system. Three patients (#13, #14 and #17) each had only one ovary available for this study. Twenty six ovaries obtained from 15 patients were diagnosed as normal and 7 ovaries obtained from 4 patients were diagnosed as malignant. One patient (#10) had her left ovary diagnosed as malignant and her right ovary diagnosed as normal. The patient category, age, mean estimated scattering coefficient, mean phase retardation and mean CAF value are summarized in Table 3-1.

Table 3-1. Patient information and measurement results.

Category	Patient No.	Age (years)	Left (L) Right(R)	Estimated scattering coefficient (mm^{-1})	Phase retardation (degrees)	Collagen area fraction (%)
Normal	#1	65	L	2.31	22.2	36.3
			R	2.12	36.6	43.8
	#2	73	L	2.38	31.0	53.6
			R	2.14	24.6	45.3
	#4	42	L	2.25	22.5	40.7
			R	2.29	16.4	53.7
	#5	55	L	2.36	24.7	58.4
			R	2.26	18.2	47.7
	#6	74	L	2.53	20.6	54.1
			R	2.29	21.2	37.1
	#7	58	L	3.00	21.7	44.2
			R	2.24	17.7	46.2
	#8	79	L	2.15	16.1	25.1
			R	2.28	23.1	46.9
	#9	79	L	2.50	25.9	42.6
			R	2.75	22.5	38.0
	#10	53	R	2.27	28.5	56.8
	#11	48	L	2.34	16.8	43.9
			R	2.35	28.2	44.6
	#12	47	L	2.47	21.3	44.6
			R	2.52	24.2	56.4
	#13	45	L	2.39	17.8	42.9
	#14	37	L	2.23	32.1	63.4
	#16	72	L	2.77	21.3	60.0
			R	2.60	17.1	39.5
	#17	48	L	2.23	15.8	30.5
	mean ± standard deviation			2.39 ± 0.21	22.6 ± 5.3	46.0 ± 9.1
Malignant	#3	77	L	1.77	31.4	32.9
			R	1.60	17.9	18.8
	#10	53	L	1.90	25.9	42.8
	#15	71	L	1.98	25.7	32.6
			R	1.10	14.7	23.3
	#18	76	L	2.16	14.7	22.0
			R	1.81	11.9	26.7
	mean ± standard deviation			1.76 ± 0.34	20.3 ± 7.4	28.4 ± 8.3

Depending on the size of the examined ovary, 34~142 measurements of scattering coefficient and phase retardation were performed for each ovary. A total of 2044 scattering coefficients and phase retardation values were estimated from these 33 ovaries while 1427 from 26 normal ones and 617 from 7 malignant ones. A total of 1072 CAFs were measured from Sirius Red staining histology while 859 from the normal group and

213 from the malignant group. The histograms of estimated scattering coefficient, phase retardation and CAF for normal and malignant groups are shown in Figure 3-5 (a)-(c), respectively. The blue bar represents the normal group and the red bar represents the malignant group. Estimated scattering coefficient in normal and malignant ovarian tissue shows Gaussian distribution property demonstrated as the dotted and solid curves in Figure 3-5 (a). The normal group has higher scattering property at a wavelength of 1310 nm ranging from 0.60 to 5.27 mm^{-1} with a mean value of 2.38 mm^{-1} (±0.67), while the malignant group demonstrates lower value ranging from 0.42 to 3.86 mm^{-1} with a mean value of 1.74 mm^{-1} (±0.55). For phase retardation shown in Figure 3-5 (b), the normal group has higher values ranging from 8.7 to 60.6 degrees with a mean value of 22.6 degrees (±9.0 degrees) while the malignant group demonstrates lower value ranging from 9.9 to 53.8 degrees with a mean value of 19.1 degrees (±9.4 degrees). For CAF shown in Figure 3-5 (c), the normal group has higher collagen content ranging from 7.6% to 81.0% with a mean value of 47.8% (±15.4%) and the malignant group has lower value ranging from 4.6% to 61.7% with a mean value of 26.2% (±11.6%). CAF in normal and malignant ovarian tissue shows Gaussian distribution property as demonstrated by dotted and solid curves in Figure 3-5 (c).

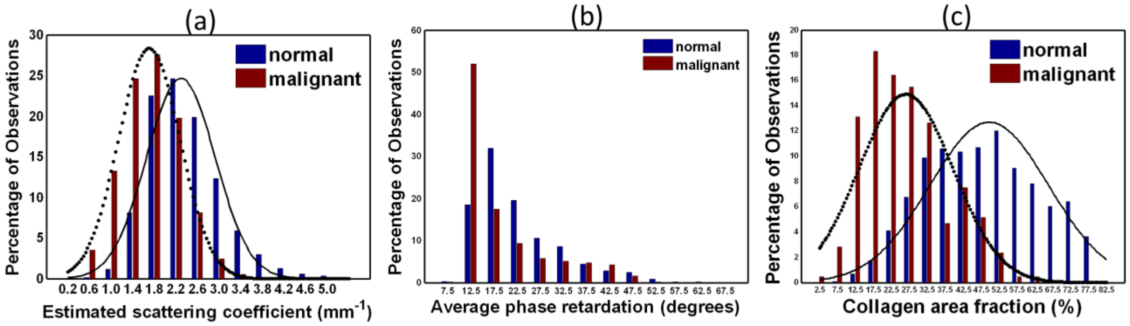

Figure 3-5. Histograms of estimated scattering coefficient (a), phase retardation (b) and collagen area fraction (c) for normal and malignant ovary groups.

The scatter plots in Figure 3-6 (a)-(c) shows mean estimated scattering coefficient, mean phase retardation and mean CAF value of each ovary for normal and malignant groups, respectively. Using estimated scattering coefficient as a classifier and selecting the separation threshold at 2 mm^{-1}, a specificity of 100% and a sensitivity of 86% are achieved. Especially for patient #10 who had left ovary diagnosed as malignant and right ovary diagnosed as normal, her bilateral ovaries are classified into correct groups based on estimated scattering coefficient. The mean value of estimated scattering coefficient of each ovary for normal and malignant groups, along with their standard deviation, is listed in Table 3-1. The Student's t-test shows statistical significance between normal and malignant groups with a p value of 0.002. Using phase retardation as a classifier and selecting the separation threshold at 15 degrees, a specificity of 100% and a sensitivity of 43% are achieved. For the two insets pointed by the dashed circle-arrows shown in Figure 3-6(b), each shows two ovaries with close values. The mean value and standard deviation of phase retardation of each ovary for normal and malignant groups are also listed in Table 3-1 and are not statistically significant ($p = 0.462$) between normal and malignant groups. However, the phase retardation images show very different features as shown in Figure 3-4 (b) and 3-4 (d) which could help characterize ovarian tissue qualitatively. In Figure 3-4 (b), the phase retardation of the normal ovarian tissue increases uniformly and is slightly dependent on the depth. But in Figure 3-4 (d), the phase retardation of the malignant ovarian tissue shows more random manner with red spots scattered in the image sporadically. Although using CAF alone as a classifier cannot completely differentiate normal from malignant ovaries (specificity 92% and sensitivity 86%) as shown in Figure 3-6 (c), statistical significance between normal

(46.0% ± 9.1%, n = 26) and malignant (28.4% ± 8.3%, n = 7) groups was found with a p value less than 0.0001.

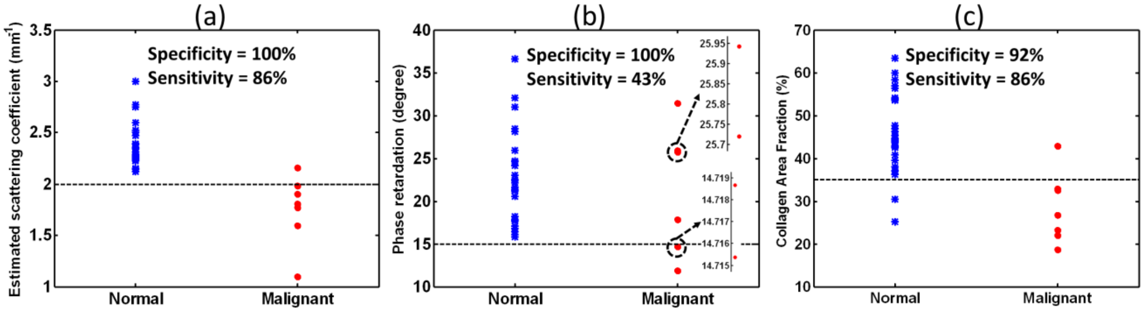

Figure 3-6. Scatter plots of estimated scattering coefficient (a), phase retardation (b) and CAF (c) of each ovary for normal and malignant ovary groups.

Combining estimated scattering coefficient and phase retardation for each ovary, we should be able to differentiate normal and malignant ovaries more effectively. The scatter plot in Figure 3-7 shows the two parameters for each ovary. The blue star represents normal ovary and the red circle represents malignant ovary. The centers and half axes of blue and red solid ellipses show the mean value and standard deviation of estimated scattering coefficient and phase retardation for each group. Using estimated scattering coefficient and phase retardation as the classifiers and selecting the same thresholds at 2 mm^{-1} and 15 degrees shown as the green dashed lines in Figure 3-7, 100% specificity and 100% sensitivity can be obtained.

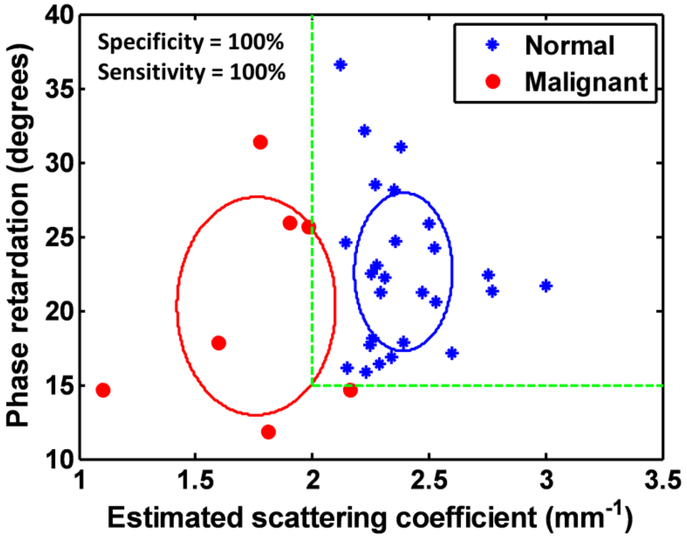

Figure 3-7. Two-parameter (estimated optical scattering coefficient and average phase retardation) plot.

Linear regression analysis in Figure 3-8 (a) shows positive correlation between collagen content and estimated scattering coefficient with R value of 0.57 ($p < 0.0001$). Phase retardation measured from ovaries is also positively correlated with collagen content with R value of 0.47 ($p < 0.01$) which is shown in Figure 3-8 (b). The blue dashed plots show the 95% prediction intervals. The different collagen content found in normal and malignant groups in part explains the different scattering properties estimated from conventional OCT measurements and the different birefringence behaviors from phase retardation images. However, there are many other factors, including collagen thickness, collagen orientation, fibroblast and cell nuclei, etc., which may need to take into account. In addition, note that in this CAF study, there are 1072 measurements which are less than the 2044 scattering coefficient and phase retardation measurements and these CAF measurements are obtained from close sites but not as exact as OCT images because it is very difficult if not impossible to exactly match the histology slides with OCT cross-section imaging planes.

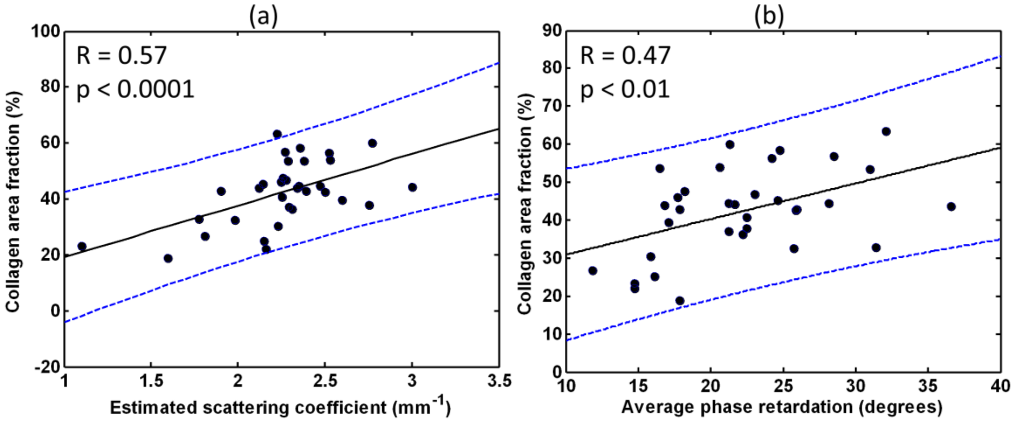

Figure 3-8. (a) Positive correlation demonstration between estimated scattering coefficient and collagen content; (b) Positive correlation demonstration between phase retardation and collagen content. The blue dashed lines show 95% prediction intervals.

It is interesting to observe from Figure 3-6 (b) and Figure 3-7 that the average phase retardation of cancer cases spreads out in a large range and a simple threshold is not adequate to separate the cancers from normal ovaries. However, a good correlation coefficient of $R = 0.7$ ($p = 0.079$) was obtained between average phase retardation and average CAF of 7 cancer cases. Because CAF from Sirius Red staining directly evaluates collagen, the positive correlation suggests the phase retardation may measure the complex collagen developmental process of ovarian cancers. Future efforts will be devoted to validating the initial results with a larger patient pool, upgrading the time domain PS-OCT system to a Fourier domain system, and developing a catheter based probe for *in vivo* inspection of ovaries during minimally invasive surgery.

3.4 Summary

In this chapter, we studied 33 ovaries obtained from 18 patients using the PS-OCT system. Optical scattering coefficient was quantitatively estimated by fitting conventional OCT signal to a single scattering model. A specificity of 100% and a sensitivity of 86% were achieved. Average phase retardation was calculated from PSOCT phase retardation image. A specificity of 100% and a sensitivity of 43% were achieved. Combining estimated scattering coefficient and phase retardation for each ovary, a superior specificity of 100% and a sensitivity of 100% were achieved. Collagen content as assessed by Sirius Red staining correlates strongly with estimated scattering coefficient and phase retardation. These initial results show PS-OCT could be a powerful tool to characterize ovarian tissue and to detect ovarian cancers.

References

1. Y. Yang*, T. Wang*, X. Wang, M. Sanders, M. Brewer, and Q. Zhu, “Quantitative analysis of estimated scattering coefficient and phase retardation for ovarian tissue characterization,” Biomed. Opt. Express 3(7), 1548-1556 (2012). (*The first two authors contributed equally to this work.)
2. Y. Yang, T. Wang, N. Biswal, X. Wang, M. Sanders, M. Brewer, and Q. Zhu, “Optical scattering coefficient estimated by optical coherence tomography correlates with collagen content in ovarian tissue,” J. Biomed. Opt. 16(9), 090504 (2011).
3. D. Huang, E. A. Swanson, C. P. Lin, J. S. Schuman, W. G. Stinson, W. Chang, M. R. Hee, T. Flotte, K. Gregory, C. A. Puliafito, and J. G. Fujimoto, “Optical coherence tomography,” Science 254, 1178-1181 (1991).
4. J. G. Fujimoto, C. Pitris, B. A. Boppart, and M. E. Brezinski, “Optical coherence tomography: an emerging technology for biomedical imaging and optical biopsy,” Neoplasia 2(1-2), 9-25 (2000).
5. A. F. Fercher, W. Drexler, C. K. Hitzenberger, and T. Lasser, “Optical coherence tomography-principles and applications,” Rep. Prog. Phys. 66(2), 239-303 (2003).
6. P. H. Tomlins and R. K. Wang, “Theory, developments and applications of optical coherence tomography,” J. Phys. D: Appl. Phys. 38(15), 2519-2535 (2005).

7. B. J. Vakoc, D. Fukumura, R. K. Jain, and B. E. Bouma, “Cancer imaging by optical coherence tomography: preclinical progress and clinical potential,” Nat. Rev. Cancer 12(5), 363-368 (2012).
8. E. M. Kanter, R. M. Walker, S. L. Marion, M. Brewer, P. B. Hoyer, J. K. Barton, “Dual modality imaging of a novel rat model of ovarian carcinogenesis,” J. Biomed. Opt. 11(4), 041123 (2006).
9. L. P. Hariri, G. T. Bonnema, K. Schmidt, A. M. Winkler, V. Korde, K. D. Hatch, J. R. Davis, M. A. Brewer, J. K. Barton, “Laparoscopic optical coherence tomography imaging of human ovarian cancer,” Gynecol. Oncol. 114(2), 188-194 (2009).
10. C. L. Evans, I. Rizvi1, T. Hasan, and J. F. de Boer, “In vitro ovarian tumor growth and treatment response dynamics visualized with time-lapse OCT imaging,” Opt. Express 17(11), 8892-8906 (2009).
11. Y. Yang, X. Li, T. Wang, P. D. Kumavor, A. Aguirre, K. K. Shung, Q. Zhou, M. Sanders, M. Brewer, and Q. Zhu, “Integrated optical coherence tomography, ultrasound and photoacoustic imaging for ovarian tissue characteruzation,” Biomed. Opt. Express 2(9), 2551-2561 (2011).
12. M. A. Brewer, U. Utzinger, J. K. Barton, J. B. Hoying, N. D. Kirkpatrick, W. R. Brands, J. R. Davis, K. Hunt, S. J. Stevens, A. F. Gmitro, “Imaging of the ovary,” Technol. Cancer Res. Treat. 3(6), 617-627 (2004).
13. Y. Yang, N. C. Biswal, T. Wang, P. D. Kumavor, M. Karimeddini, J. Vento, M. Sanders, M. Brewer, and Q. Zhu, “Potential role of a hybrid intraoperative probe based on OCT and positron detection for ovarian cancer detection and characterization,” Biomed. Opt. Express 2(7), 1918-1930 (2011).
14. M. R. Hee, D. Huang, E. A. Swanson, and J. G. Fujimoto, “Polarization-sensitive low-coherence reflectometer for birefringence characterization and ranging,” J. Opt. Soc. Am. B 9(6), 903-908 (1992).
15. J. F. de Boer, T. E. Milner, M. J. C. van Gemert, and J. S. Nelson, “Two-dimensional birefringence imaging in biological tissue by polarization-sensitive optical coherence tomography,” Opt. Lett. 22(12), 934-936 (1997).
16. B. Cense, T. C. Chen, B. H. Park, M. C. Pierce, and J. F. de Boer, “Thickness and birefringence of healthy retinal nerve fiber layer tissue measured with polarization-sensitive optical coherence tomography,” Invest. Ophthalmol. Vis. Sci. 45(8), 2606-2612 (2004).
17. B. Elmaanaoui, B. Wang, J. C. Dwelle, A. B. McElroy, S. S. Liu, H. G. Rylander, and T. E. Milner, “Birefringence measurement of the retinal nerve fiber layer by swept source polarization sensitive optical coherence tomography,” Opt. Express 19(11), 10252-10268 (2011).
18. M. C. Pierce, R. L. Sheridan, B. H. Park, B. Cense, and J. F. de Boer, “Collagen denaturation can be quantified in burned human skin using polarization-sensitive optical coherence tomography,” Burns. 30, 511-517 (2004).
19. J. Strasswimmer, M. C. Pierce, B. H. Park, V. Neel, and J. F. de Boer, “Polarization-sensitive optical coherence tomography of invasive basal cell carcinoma,” J. Biomed. Opt. 9(2), 292-298 (2004).
20. S. Sakai, M. Yamanari, A. Miyazawa, M. Matsumoto, N. Nakagawa, T. Sugawara, K. Kawabata, T. Yatagai, and Y. Yasuno, “In vivo three-dimensional birefringence

analysis shows collagen differences between young and old photo-aged human skin," J. Invest. Dermatol. 128, 1641-1647 (2008).

21. S. K. Nadkarni, M. C. Pierce, B. H. Park, J. F. de Boer, P. Whittaker, B. E. Bouma, J. E. Bressner, E. Halpern, S. L. Houser, and G. J. Tearney, "Measurement of collagen and smooth muscle cell content in atherosclerotic plaques using polarization-sensitive optical coherence tomography," J. Am. Coll. Cardiol. 49(13), 1474-1481 (2007).
22. W. Kuo, N. Chou, C. Chou, C. Lai, H. Huang, S. Wang, and J. Shyu, "Polarization-sensitive optical coherence tomography for imaging human atherosclerosis," Appl. Opt. 46(13), 2520-2527 (2007).
23. D. Fried, J. Xie, S. Shafi, J. D. B. Featherstone, T. M. Breunig, and C. Le, "Imaging caries lesions and lesion progression with polarization sensitive optical coherence tomography," J. Biomed. Opt. 7(4), 618-627 (2002).
24. Y. Chen, L. Otis, D. Piao, and Q. Zhu, "Characterization of dentin, enamel, and carious lesions by a polarization-sensitive optical coherence tomography system," Appl. Opt. 44(11), 2041-2048 (2005).

4 A three-parameter logistic model for ovarian cancer detection using polarization-sensitive optical coherence tomography [1]

4.1 Introduction

Polarization-sensitive OCT (PS-OCT) is a functional extension of OCT [2-7] and capable of detecting birefringence changes caused by collagen, and collagen changes in human ovary are indicators of malignancy [8,9]. Therefore, PS-OCT could be an effective tool to detect ovarian cancer. In chapter 3, optical scattering coefficient and phase retardation of 33 *ex vivo* ovaries obtained from 18 patients were extracted from time domain (TD) PS-OCT intensity and phase images, respectively [10]. While the scattering coefficient was significant in predicting malignancy, the phase retardation achieved low sensitivity of 43%. In this study, a more sensitive parameter, the phase retardation rate, was extracted from PS-OCT phase images and used together with the scattering coefficient and phase retardation to characterize ovarian tissue. In the literature, the PS-OCT phase retardation rate was introduced by M. C. Pierce et al. to quantify collagen denaturation in burned human skin [11]. In our study, these three parameters extracted from 33 ovaries were used as inputs to a logistic model to predict or classify the malignant and benign ovaries. In addition, 10 more ovaries from 5 patients were imaged with our upgraded Fourier domain (FD) PS-OCT system and used to test the model. To the best of our knowledge, this is the first study of using multiple parameters extracted from PS-OCT images as predictors for ovarian tissue characterization.

4.2 Materials and methods

4.2.1 Ovary sample and histopathology

A total of 43 ovaries were extracted from 23 patients undergoing PO at the University of Connecticut Health Center (UCHC). 33 ovaries from 18 patients were imaged using TD-PS-OCT while 10 ovaries from 5 patients were imaged using FD-PS-OCT. These patients were at risk for ovarian cancer or they had ovarian mass or pelvic mass suggesting malignancy. This study was approved by the Institutional Review Board of UCHC, and informed consent was obtained from all patients. The details of imaging procedures and histological processing were described in chapter 3. Sirius Red staining protocol was applied to the sectioned slides to analyze the collagen content. The amount of collagen was quantitatively analyzed using ImageJ software (National Institute of Health). The average collagen area fraction (CAF) was measured as “Stained collagen area/tissue area”.

4.2.2 PS-OCT systems

The TD-PS-OCT and upgraded FD-PS-OCT systems are shown in Figure 4-1 (a). The essential optical configurations of the TD-PS-OCT and upgraded FD-PS-OCT systems are the same. The technical details of the TD-PS-OCT system were described in chapter 3. The main differences between the upgraded FD system and the TD system are:

(1) the super luminescent diode source was replaced with an 110 nm bandwidth swept source (HSL-2000, Santec Corp., Japan) with center wavelength of 1310 nm and scan rate of 20 kHz; (2) the detectors were replaced with 75MHz bandwidth photodetectors (Thorlabs PDB120C); (3) the reference mirror was fixed instead of moving back and forth by a stepper motor. The conventional OCT intensity images were obtained from calculating the summation of squares of two orthogonally polarized signals, and the phase retardation images were obtained by calculating arctangent between vertical and horizontal polarization components [12].

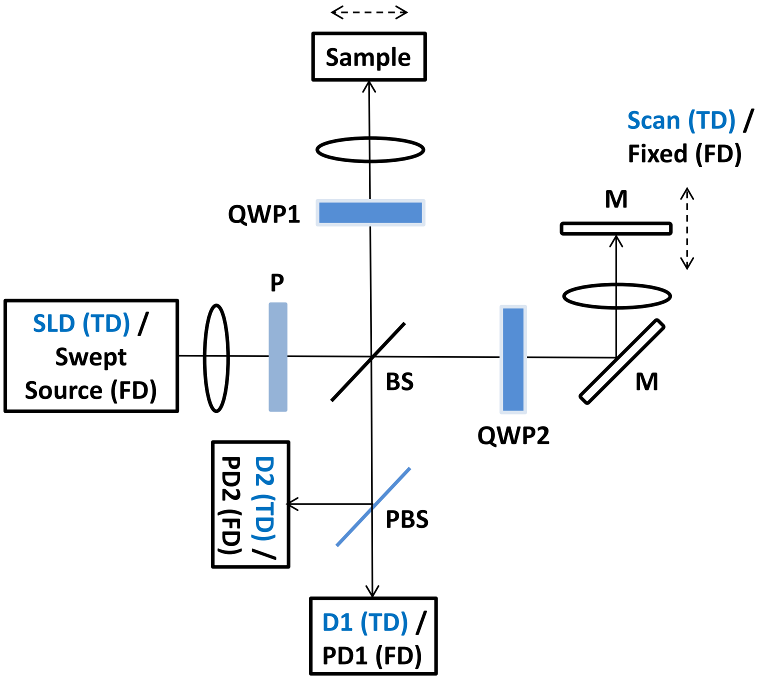

Figure 4-1. TD/FD-PS-OCT systems configuration. P: polarizer; BS: beam splitter; PBS: polarization beam splitter; QWP: quarter-wave plate; M: mirror; PD: photodetector.

4.2.3 Phase retardation rate

During imaging, similar conditions for all ovary samples were obtained by mounting the ovary on a three-dimensional stage and adjusting the ovarian tissue surface to the same depth position. The phase retardation rate was obtained by linearly fitting phase retardation depth profile. The region of interest (ROI) selection was consistent with that in chapter 3 when calculating scattering coefficient and phase retardation. Overall, each image was evenly divided into several ROIs with 1mm width. Values in all ROIs from all images of one ovary were averaged to obtain the phase retardation rate of this ovary. The same procedures were followed for all ovaries. An example of fitting phase retardation rate of a normal ovary is shown in Figure 4-2 (a) and 4-2 (b). Figure 4-2 (a) is the phase retardation image, where the dark blue represents phase retardation value of zero degree and the dark red represents 90 degrees. The white dashed rectangular area was selected for fitting. The depth profile of the averaged A-lines in the selected area was shown as blue curve in Figure 4-2 (b), and the numerical fitting curve was plotted as red. The slope of the red curve was calculated as the phase retardation rate. The phase retardation decreases with depth after about 1.5mm. This is because the ratio of vertical and horizontal signals reduces as light penetrates deeper in the tissue. The fitting error of the phase retardation rate is estimated as the norm of the fitting residue divided by the norm of the original curve.

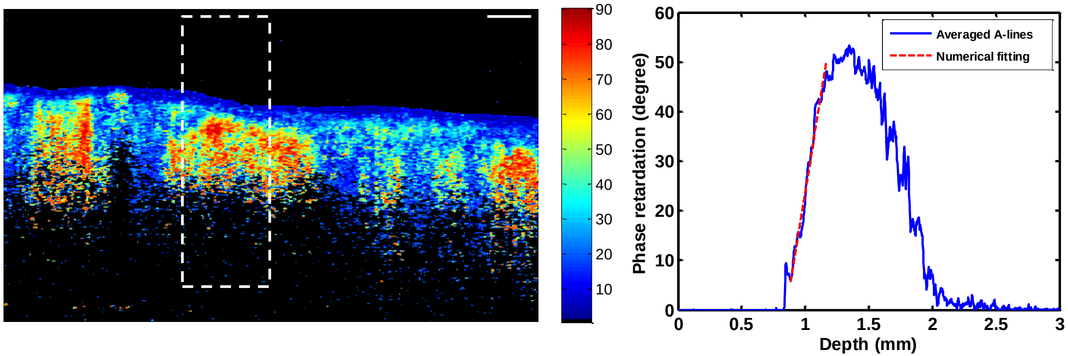

(a) (b)

Figure 4-2. Example of calculating the phase retardation rate. (a) Phase retardation image; white dashed rectangular: selected area for fitting; scale bar: 0.5mm; (b) averaged A-lines and numerical fitting curves.

4.2.4 Optical scattering coefficient and phase retardation

The quantification of scattering coefficient and phase retardation were described in chapter 3. Scattering coefficient was estimated by numerically fitting compounded conventional OCT depth profile to a single scattering model based on Beer's law. 1mm tissue was averaged to minimize the speckle noise. The phase retardation was obtained by calculating the average phase values from PS-OCT phase images of the same area.

4.2.5 Logistic model and receiver operating characteristic curve

Logistic regression belongs to the class of generalized linear model (GLM) based on the exponential distribution family. It is a statistical model that can describe the relationship of several predictor variables X_1, X_2, …, X_k to a dichotomous response variable Y (0 or 1) [13]. The probability of occurrence of one of the two possible outcomes of Y can be described by the following equation:

$$pr(Y=1 \mid X_1, X_2, \ldots, X_K) = \frac{1}{1+\exp\left[-\left(\beta_0 + \sum_{n=1}^{k} \beta_n X_n\right)\right]} \tag{4-1}$$

Given the data Y, X_1, X_2, …, X_k, the unknown coefficients $\beta_n, n = 0,1,\ldots,k$ can be estimated using the maximum likelihood method. In this paper, we use three predictors (scattering coefficient, phase retardation, and phase retardation rate) to classify normal and malignant ovarian tissue. The MATLAB GLMFIT function was used to fit the logistic model using the predictors and the response (0 represents normal and 1 represents malignant). The coefficients $\beta_n, n = 0,1,\ldots,k$ of the model that best follow the actual diagnosis were estimated and used to calculate the estimated responses (the numbers between 0 and 1) using GLMVAL function. The GLMFIT function also computed the deviance, which is a generalization of the residual sum of squares (comparison of log-likelihood function of actual fitted values with perfectly fitted values). The deviance was used to compare different prediction models, in which different parameter-combinations were used as predictors to classify normal and malignant ovaries. The deviance value decreases as the model fit improves.

The quality of the logistic prediction model was evaluated using the area under the receiver operating characteristic (ROC) curve (AUC). The estimated responses from different prediction models were used to compute the ROC curves and AUCs using R package pROC [14]. We also estimated the 95% confidence interval (CI) using bootstrap method with 10,000 stratified bootstrap replicates. The optimal threshold provided by pROC was used to calculate the sensitivity and specificity, positive and negative predictive values (PPV, NPV). To further evaluate the logistic prediction model and testing results, we have also investigated the correlation coefficients R_{train} and R_{test} between calculated responses and the actual diagnosis (0 normal and 1 malignant).

4.3 Results and discussion

4.3.1 Statistical results of 33 ovaries imaged by TD-PS-OCT

A total of 33 *ex vivo* ovaries from 18 patients were imaged using TD-PS-OCT system. 26 ovaries were diagnosed as normal and 7 ovaries were diagnosed as malignant. Figure 4-3 shows box plots and p values of normal and malignant ovary groups. Normal ovaries show higher average values of scattering coefficient and phase retardation than malignant ones, with the normal/malignant ratio of 1.36, 1.11, respectively. For phase retardation rate, the average fitting range of normal group is 36.7-329.8 μm from the tissue surface, and the malignant group is 38.4-347.3 μm. The range of average value of normal group is 28.8-154.8 degree/mm, and malignant group is 8.4-121.6 degree/mm. The normal group has mean value of 79.5 degrees/mm (±19.0), which is higher than that of the malignant group with mean value of 45.0 degrees/mm (±19.6). The normal/malignant ratio of phase retardation rate is 1.77. Phase retardation rate of normal and malignant ovaries shows larger difference ($p<0.0001$) than the other two parameters. The fitting error of the phase retardation rate of the normal and the malignant group is 5.13% (±0.82%) and 4.69% (±0.96%), respectively.

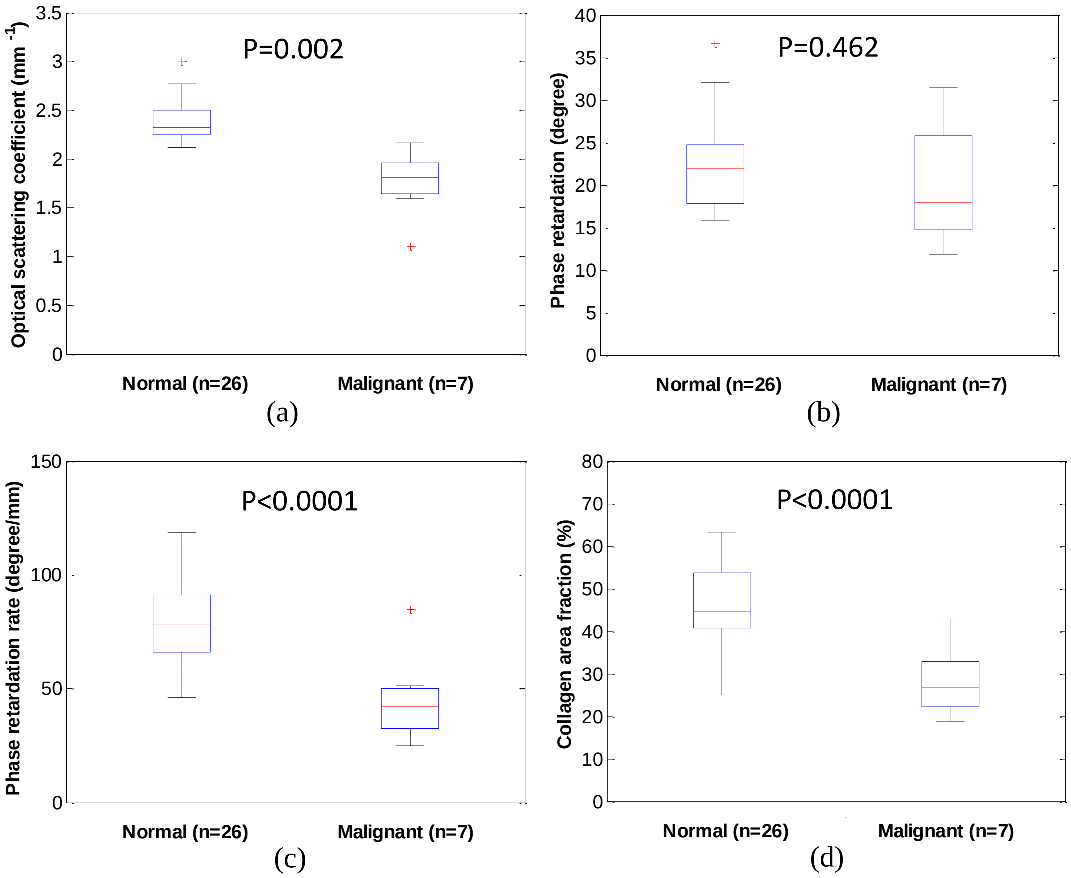

(a) (b)

(c) (d)

Figure 4-3. Box plots of normal and malignant ovary groups. (a) Optical scattering coefficient; (b) phase retardation; (c) phase retardation rate; (d) collagen area fraction.

The scatter plot in Figure 4-4 (a) shows the average phase retardation rate of each ovary for normal and malignant groups. The blue star represents the normal ovaries and the red circle represents the malignant ones. By setting a threshold of phase retardation rate at the value of 55 degree/mm, we could achieve 85.7% sensitivity and 92.3% specificity. However, by using phase retardation as a classifier, we could only achieve 42.9% sensitivity. These results indicate that phase retardation rate could be a more significant parameter than phase retardation in distinguishing normal from malignant ovaries. Linear regression analysis is shown in Figure 4-4 (b). A positive correlation was found between phase retardation rate and collagen content, with Pearson's correlation coefficient R=0.74 (p<0.0001), which is higher than those from scattering coefficient (R=0.57, p<0.0001) and phase retardation (R=0.47, p<0.01). A multiple linear regression shows that those three parameters together positively correlate with collagen content with R=0.76, which is higher than that using each parameter alone. Collagen is associated with the development of ovarian cancers; the collagen amount and structure are quite different between normal and malignant ovaries. The normal and malignant groups have CAF values of 46.0% (±9.1%), and 28.4% (±8.3%), respectively. Since CAF, measured from Sirius Red staining on ovary samples, directly assesses collagen, the highly positive correlation indicates that the phase retardation rate may measure the complicated process of collagen development of ovarian cancer.

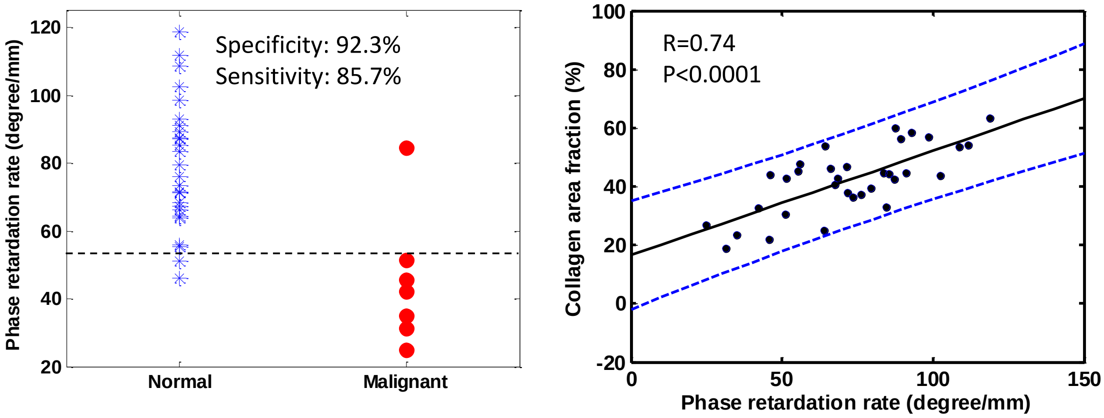

(a) (b)

Figure 4-4. (a) Scatter plot of phase retardation rate of normal and malignant ovary groups. (b) Positive correlation demonstration between phase retardation rate and collagen content; the blue dashed lines show 95% confidence interval.

4.3.2 Training results based on logistic model using the 33-ovary data

The three parameters extracted from 33-ovary images were used to train the logistic classifier. As shown by the ROC curves in Figure 4-5, the use of all three parameters shows much better performance than each parameter alone. The more specific prediction results, including sensitivity, specificity, PPV, NPV, AUC (95% CI), correlation coefficient R_{train} between estimated responses and actual responses (p value), and deviance, of different parameter-combinations are summarized in Table 4-1. By using only one parameter as a predictor, none of the models could achieve perfect sensitivity and specificity. By using combinations of any two parameters except one set using phase retardation and phase retardation rate, or using three parameters as predictors, 100% sensitivity and specificity are achieved. The deviance of using three parameters together is smaller than that of using two parameters, which indicates that the three-parameter model is more reliable.

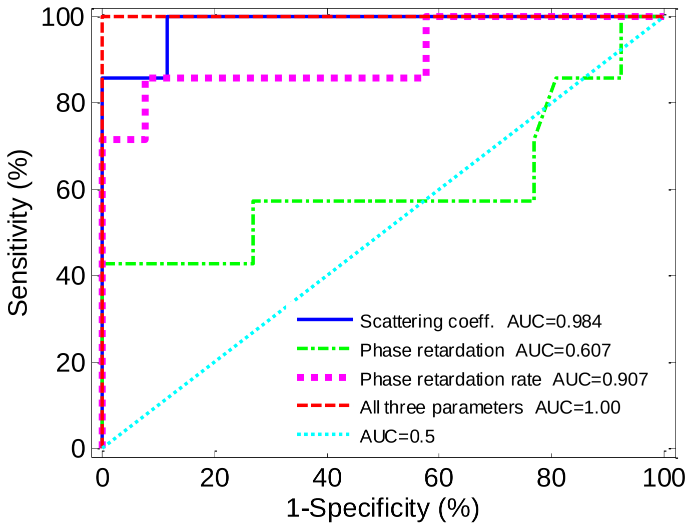

Figure 4-5. ROC curves and AUC of different prediction models: training results.

Table 4-1. Summary of logistic model results by using different parameters. SC: scattering coefficient, PR: phase retardation, PRR: phase retardation rate, Th: threshold.

Prediction model (Th)	**Sensitivity**	**Specificity**	**PPV**	**NPV**	**AUC (95% CI)**	**R_{train} (p value)**	**Deviance**
SC (0.65)	85.7%	100%	100%	96.3%	0.984 (0.934:1.0)	0.911 (<0.0001)	5.94
PR (0.30)	42.9%	100%	100%	86.7%	0.607 (0.302:0.885)	0.212 (0.237)	33.14
PRR (0.38)	85.7%	92.3%	75.0%	96.0%	0.907 (0.720:1.0)	0.747 (<0.0001)	18.92
SC+PR (0.50)	100%	100%	100%	100%	1.000 (1.0:1.0)	1.000 (<0.0001)	6.22e-13
SC+PRR (0.50)	100%	100%	100%	100%	1.000 (1.0:1.0)	1.000 (<0.0001)	1.94e-14
PR+PRR (0.18)	100%	92.3%	77.0%	100%	0.973 (0.912:1.0)	0.774 (<0.0001)	13.30
SC+PR+PRR (0.50)	100%	100%	100%	100%	1.000 (1.0:1.0)	1.000 (<0.0001)	1.60e-14

4.3.3 Testing results of 10 ovaries imaged by FD-PS-OCT

10 ovaries (6 normal and 4 malignant) from 5 patients were imaged using the upgraded FD system and were tested using logistic prediction model based on different parameters described above. The testing results are summarized in Table 4-2. The same threshold of the training group was used for this testing group to calculate the sensitivity, specificity, PPV, and NPV. The R_{test} values are also shown in Table 4-2 to compare different prediction models. The R_{test} and AUC are highest (R_{test} =0.893, p<0.001, AUC=1.0) when using the three-parameter prediction model. Note that the three-

parameter model achieved AUC=1 as shown in Figure 4-6, but the sensitivity (100%) and specificity (83.3%) are not perfect. This is because we set a threshold of 0.5 for the training and testing groups for classifying normal and malignant ovaries. If we set a threshold of 0.7, we could achieve 100% sensitivity and specificity. However, in the three-parameter model training, all estimated responses of normal cases are very close to normal response 0, and all estimated responses of malignant cases are very close to malignant response 1, so it makes more sense to set the middle point 0.5 as a threshold based on the training results.

Table 4-2. Summary of testing results by using the same threshold of the training group. SC: scattering coefficient, PR: phase retardation, PRR: phase retardation rate, Th: threshold.

Prediction model (Th)	**Sensitivity**	**Specificity**	**PPV**	**NPV**	**AUC (95% CI)**	**R_{test} (p value)**
SC (0.65)	75.0%	83.3%	75.0%	83.3%	0.958 (0.833:1.0)	0.764 (0.010)
PR (0.30)	0%	100%	0%	60.0%	0.917 (0.667:1.0)	0.624 (0.054)
PRR (0.38)	50.0%	100%	100%	75.0%	0.958 (0.833:1.0)	0.751 (0.012)
SC+PR (0.50)	75.0%	100%	100%	85.7%	0.875 (0.625:1.0)	0.802 (0.005)
SC+PRR (0.50)	100%	83.3%	80.0%	100%	0.958 (0.750:1.0)	0.789 (0.007)
PR+PRR (0.18)	75.0%	83.3%	75.0%	83.3%	0.833 (0.500:1.0)	0.495 (0.146)
SC+PR+PRR (0.50)	100%	83.3%	80.0%	100%	1.000 (1.0:1.0)	0.893 (<0.001)

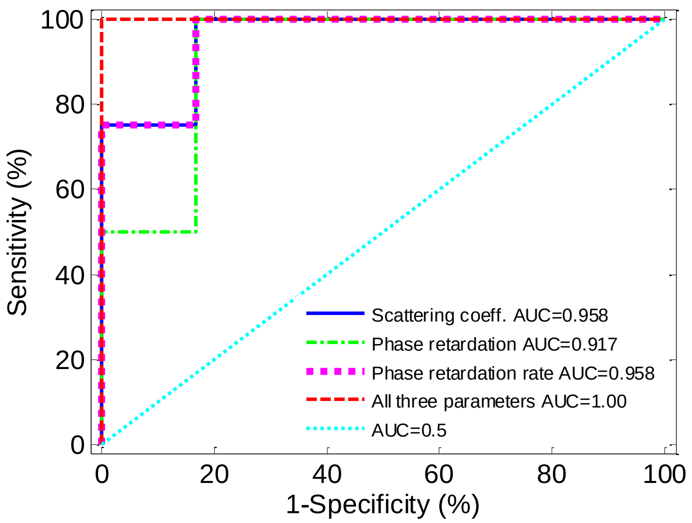

Figure 4-6. ROC curves and AUC of different prediction models: testing results.

In this study, only 10 ovaries were tested using our logistic model, more ovary data will be collected to validate the initial results. Currently, because all parameter extraction and processing are offline, future work also includes automating our data processing procedures so that we could obtain these parameters and input them to the prediction model in real-time.

4.4 PS-OCT based on polarization-maintaining fiber

Free-space PS-OCT system is bulky compared with fiber-based system. For translating this technique from bench to bedside, a more compact fiber-based Fourier-domain PS-OCT system is developed. The system configuration is shown is Figure 4-7. The PS-OCT system consists of a swept source at center wavelength of 1310 nm and a fiber-based Michelson interferometer. The light beam from the swept source passes an in-line fiber polarizer and is evenly separated into sample arm and reference arm by a 50/50 polarization-maintaining (PM) fiber coupler. In the sample arm, a quarter-waveplate

QWP1 with the fast axis oriented at 45 degrees with respect to the horizontal direction is used to convert the linearly polarized light into the circularly polarized light. The circularly polarized light is focused on the examined sample through an objective lens. In the reference arm, another quarter-waveplate QWP2 with the fast axis oriented at 22.5 degrees with respect to the horizontal direction is placed after the PM fiber coupler. After light beam back-propagating through the QWP2, the polarization state is changed to 45 degrees with respect to the horizontal direction which provides equal reference power for both orthogonal polarization channels. The backscattered beam from the sample arm and the back-reflected beam from reference arm recombine and interfere at the PM fiber coupler. The recombined light is separated by a polarization beam splitter (PBS) into horizontal and vertical components which are detected by two identical photodetectors (BD1 and BD2). Same as the free-space PS-OCT, the conventional OCT image is obtained by calculating the summation of the squares of both orthogonal polarization channel signals; phase retardation image is obtained from measuring the arctangent between vertical and horizontal components.

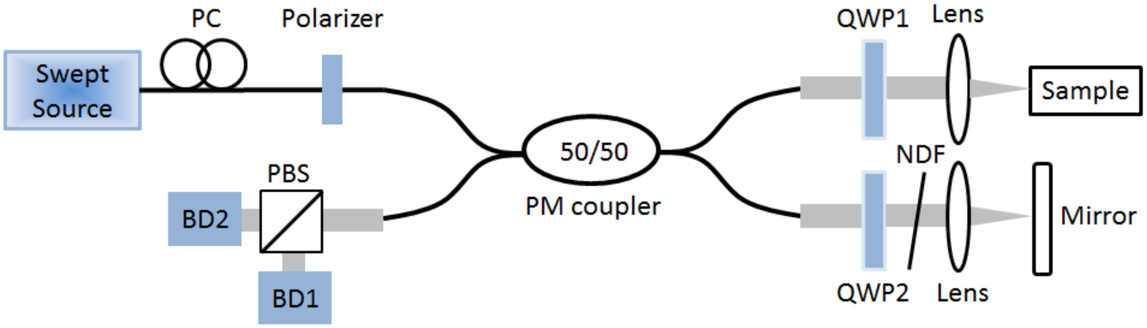

Figure 4-7. Fiber-based PS-OCT system configuration. PC: polarization controller; PM: polarization-maintaining; QWP: quarter waveplate; NDF: neutral density filter; PBS: polarization beam splitter.

Figure 4-8 shows the human ovarian tissue images acquired by this fiber-based PS-OCT system, where Figure 4-8 (a) is the OCT intensity image and Figure 4-8 (b) is the phase retardation image.

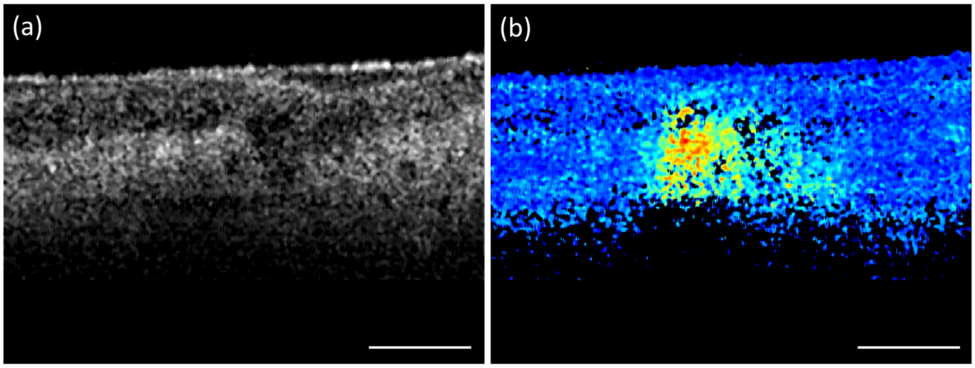

Figure 4-8. Conventional OCT (a) and phase retardation image (b) of human ovarian tissue. Scale bar: 0.5 mm.

4.5 Summary

The phase retardation rate quantitatively extracted from PS-OCT has significantly improved the ovarian cancer diagnosis when it is used together with optical scattering coefficient and phase retardation. By using a new three-parameter logistic prediction model, we achieve 100% sensitivity and specificity in the training group, and 100% sensitivity and 83.3% specificity in the testing group. The initial results demonstrate that the three-parameter prediction model based on PS-OCT could be a powerful tool to evaluate ovarian tissue.

References

1. T. Wang, Y. Yang, and Q. Zhu, “A three-parameter logistic model to characterize ovarian tissue using polarization-sensitive optical coherence tomography,” Biomed. Opt. Express 4(5), 772-777 (2013).

2. M. R. Hee, D. Huang, E. A. Swanson, and J. G. Fujimoto, “Polarization-sensitive low-coherence reflectometer for birefringence characterization and ranging,” J. Opt. Soc. Am. B 9(6), 903-908 (1992).
3. J. F. de Boer, T. E. Milner, M. J. C. van Gemert, and J. S. Nelson, “Two-dimensional birefringence imaging in biological tissue by polarization-sensitive optical coherence tomography,” Opt. Lett. 22(12), 934-936 (1997).
4. S. K. Nadkarni, M. C. Pierce, B. H. Park, J. F. de Boer, P. Whittaker, B. E. Bouma, J. E. Bressner, E. Halpern, S. L. Houser, and G. J. Tearney, “Measurement of collagen and smooth muscle cell content in atherosclerotic plaques using polarization-sensitive optical coherence tomography,” J. Am. Coll. Cardiol. 49(13), 1474-1481 (2007).
5. S. Sakai, M. Yamanari, A. Miyazawa, M. Matsumoto, N. Nakagawa, T. Sugawara, K. Kawabata, T. Yatagai, and Y. Yasuno, “In vivo three-dimensional birefringence analysis shows collagen differences between young and old photo-aged human skin,” J. Invest. Dermatol. 128, 1641-1647 (2008).
6. M. K. Al-Qaisi and T. Akkin, “Swept-source polarization-sensitive optical coherence tomography based on polarization-maintaining fiber,” Opt. Express 18(4), 3392-3403 (2010).
7. B. Elmaanaoui, B. Wang, J. C. Dwelle, A. B. McElroy, S. S. Liu, H. G. Rylander, and T. E. Milner, “Birefringence measurement of the retinal nerve fiber layer by swept source polarization sensitive optical coherence tomography,” Opt. Express 19(11), 10252-10268 (2011).
8. M. A. Brewer, U. Utzinger, J. K. Barton, J. B. Hoying, N. D. Kirkpatrick, W. R. Brands, J. R. Davis, K. Hunt, S. J. Stevens, and A. F. Gmitro, “Imaging of the ovary,” Technol. Cancer Res. Treat. 3(6), 617-627 (2004).
9. Y. Yang, T. Wang, N. C. Biswal, X. Wang, M. Sanders, M. Brewer, and Q. Zhu, “Optical scattering coefficient estimated by optical coherence tomography correlates with collagen content in ovarian tissue,” J. Biomed. Opt. 16(9), 090504 (2011).
10. Y. Yang, T. Wang, X. Wang, M. Sanders, M. Brewer, and Q. Zhu, “Quantitative analysis of estimated scattering coefficient and phase retardation for ovarian tissue characterization,” Biomed. Opt. Express 3(7), 1548-1556 (2012).
11. M. C. Pierce, R. L. Sheridan, B. H. Park, B. Cense, and J. F. de Boer, “Collagen denaturation can be quantified in burned human skin using polarization-sensitive optical coherence tomography,” Burns 30, 511-517 (2004).
12. Y. Chen, L. Otis, D. Piao, and Q. Zhu, “Characterization of dentin, enamel, and carious lesions by a polarization-sensitive optical coherence tomography system,” Appl. Opt. 44(11), 2041-2048 (2005).
13. D. Kleinbaum, L. Kupper, K. Muller, and A. Nizam, “Applied regression analysis and other multivariable methods,” Duxbury Press, Third Edition (1998).
14. X. Robin, N Turck, A. Hainard, N. Tiberti, F. Lisacek, J. Sanchez, and M. Müller , “pROC: an open-source package for R and S+ to analyze and compare ROC curves,” BMC Bioinformatics 12(77), 1-8 (2011).

5 Application of laser pulse stretching scheme for efficiently delivering laser energy in photoacoustic imaging [1]

5.1 Introduction

Photoacoustic imaging has emerged as a promising biomedical imaging technique and demonstrated great potential for medical applications [2,3], including imaging skin tissue [4], brain vasculature [5-7], cancerous lesions in the breast [8] and ovarian tissue [9,10]. Near-infrared short-pulsed laser light is employed for tissue irradiation and an ultrasound transducer is used to receive the photoacoustic signals generated by the tissue from absorption of the light. In many clinical applications, including intravascular probe [11,12], endoscopy [13], and transvaginal photoacoustic probe for noninvasive ovarian cancer screening [10], optical fibers are widely used to deliver the laser beam to the imaged tissue. During the photoacoustic imaging of deeply-seated lesions lying several centimeters below the tissue surface, high-energy and short duration laser pulses are often employed to improve the image quality. These high peak intensity pulses can however damage an optical fiber input face during light coupling if the fiber damage threshold is exceeded [14]. This in turn limits the total energy that can be coupled into optical fibers for delivering the laser light to the imaged tissue. For deeply-seated lesions in particular, the limited energy imposed by the fiber damage threshold could result in poor image quality and contrast. Beyrau et al. [15] indicated that the damage threshold for fused silica was 1

GW/cm^2. Robinson et al. [16] reported the peak power damage threshold of various commercial fibers at the laser wavelength of 532 nm and the pulse width of 10ns. The measured damage threshold varied from 3.7 GW/cm^2 for a 100 μm-core-diameter fiber to 3.9 GW/cm^2 for a 200 μm-core-diameter fiber, and the corresponding pulse energy damage threshold varied from 2.9 mJ to 9.7 mJ. They also reported that the damage threshold of their experimental 700 μm fiber was 0.86 GW/cm^2 which was similar to the 1 GW/cm^2 damage threshold level of the commercially available high energy fiber from OFS Inc (Fitel HCGMO200T 200 μm). For the *in vivo* clinical applications, including the intravascular and endoscopic photoacoustic imaging, the probe needs to be miniaturized and the fiber diameters need to be in the range of a few hundred micrometers [11,13]. Also, in photoacoustic imaging, the laser pulse width is usually as low as 5-7 ns [11,13,17]. Assuming the laser pulse width is 6 ns and the fiber diameter is 400 μm, based on the 1GW/cm^2 fiber damage threshold [15,16], the maximum energy that can be coupled into the fiber is only about 7.5 mJ; if the fiber diameter is 200 μm, the maximum energy coupled is only about 1.9 mJ. Considering the coupling loss of optical fibers, the output energy would be even lower, which is far below the maximum permissible exposure (MPE) [18] and not enough for imaging deeper lesions. Therefore, increasing the fiber damage threshold is a critical issue for photoacoustic imaging applications.

The coreless fiber endcap can also reduce the optical damage at fiber end faces, and the anti-reflective (AR) coating can minimize the back-reflection. However, the fiber endcap and the AR coating can cause extra energy losses including splicing loss. Moreover, the damage threshold is highly dependent on how the interface is prepared. Therefore the improvement on the fiber damage threshold is not predictable. In reference

16, a tapered glass funnel was used to couple the laser light to a hollow glass waveguide. The maximum input energy was increased, but the total laser energy delivery efficiency was only 30%. Besides, the delivery system was complicated and the coupling was a variable, and its cost was much higher than that for commercial silica fibers. Comparing with those methods, laser-pulse-stretching is a convenient and an effective technique to solve the fiber damage problem. It can reduce the peak power and increase the fiber damage threshold [19]. Ideally, the laser pulse can be stretched without losing optical energy. Pulse stretching techniques include optical pulse stretching [20-23], electronic pulse stretching [24, 25], pulse stretching by dispersion [26-28], and pulse stretching using nonlinear materials [29, 30]. In optical pulse stretching, optical components are used to split the incident laser pulse into two or more pulses, and an appropriate optical delay is introduced to each pulse. Recombination of all the delayed pulses then results in a stretched pulse. One typical example of an optical pulse stretching system is the ring cavity configuration using mirrors and beam-splitters. A square ring cavity was reported in an oscillator-amplifier copper vapor laser which stretched the laser pulse from 34 ns to 50 ns [20]. Multiple-ring-cavity configuration was reported to stretch the 8.4 ns laser pulse of Q-switched Nd:YAG laser to a 75 ns laser pulse with a peak power reduction to 10% and an efficiency of 83% [21]. An optical pulse stretcher composed of two optical cavities was reported to stretch a 24 ns laser pulse and also realized fast switching between different pulse durations (24 ns, 60 ns, 63 ns, 122 ns) [22]. Among those methods of pulse stretching, the ring-cavity setup is easy and the cost is low.

In this chapter, the effect of pulse stretching on photoacoustic imaging is studied by simulations and experiments. An initial 17 ns laser pulse measured at the half maximum

(FWHM) was launched from a Ti:sapphire laser and stretched to 27 ns and 37 ns by a ring-cavity nanosecond laser pulse stretching system in order to increase the fiber damage threshold. The peak of the 37 ns stretched pulse reduced to 42% of the original pulse and the stretched pulse increased the fiber damage threshold by 1.5-fold, which is significant in delivering higher total energy for deep tissue imaging. Photoacoustic signals from different target sizes obtained with different pulse durations were simulated. Three ultrasound transducers centered at 1.3 MHz, 3.5 MHz, 6 MHz frequencies of 120%, 80%, 80% fractional bandwidth were used. The simulations were validated by experimental results using a broadband hydrophone with a flat frequency response from 1 to 10 MHz. In addition, quantitative comparisons of photoacoustic images obtained with three ultrasound transducers of the same center frequency and bandwidth as the simulation showed that the image quality was not affected by stretching the pulse using the reported ring-cavity technique. To the best of our knowledge, this is the first study applying laser pulse stretching to photoacoustic imaging applications. The simulations and experimental results can be used as a reference for laser pulse stretcher designs on compromising total energy delivery to tissue and fiber damage threshold.

5.2 Methods

5.2.1 Simulation method

The MATLAB k-Wave toolbox [31] was used to simulate the time-domain photoacoustic signal and the fast Fourier transform (FFT) was applied to obtain the frequency domain spectrum. The k-Wave simulation functions are based on a k-space pseudo-spectral time domain solution to couple first-order acoustic equations for homogenous and heterogeneous media. In our k-Wave simulations, a Gaussian pulse beam was uniformly applied to a disc target and a single-element sensor was used to detect the acoustic wave within a two-dimensional homogeneous medium. To simulate the effects of the limited bandpass of the transducers, different Gaussian bandpass filers were applied to the frequency domain of the simulated time-domain photoacoustic signals. Three different ultrasound transducers of center frequencies of 1.3 MHz, 3.5 MHz and 6 MHz with fractional bandwidths of 120%, 80%, 80%, respectively, were used in the simulations. Transducers in the central frequency range of 3 MHz-10 MHz are typically used in clinical ultrasound systems. Transducers in the lower frequency range of 1-2 MHz are often used by the research community for photoacoustic imaging applications.

5.2.2 Ring-cavity pulse stretching system

One way to achieve the objective of reducing the laser peak intensity with only a minimal energy loss is to use the pulse stretcher realized by an optical triangular ring cavity [21]. As shown in Figure 5-1, an initial input laser pulse $I_0(t)$ is partially reflected by a fractional amount of R_{BS} and partially transmitted by (1-R_{BS}) through the beam splitter, where R_{BS} is the reflectivity of the beam splitter. This transmitted pulse circulates inside the ring cavity and is then reflected and transmitted again and again by the beam splitter. The successive laser pulses from the ring cavity have optical delay times of τ, 2τ, …, $k\tau$, where k is an integer which represents the number of round trips in the ring cavity.

As a result, the initial input laser pulse is divided into many pulses with different optical delay times, so the output laser pulse *I(t)* is given by the superposition of each smaller amplitude pulses to achieve the pulse stretching. This is shown by the equation:

$$\begin{aligned} I(t) &= R_{BS} I_0(t) + (1-R_{BS})^2 I_0(t-\tau) + (1-R_{BS})^2 R_{BS} I_0(t-2\tau) + \cdots \\ &= R_{BS} I_0(t) + (1-R_{BS})^2 \sum_{k=1}^{K} R_{BS}^{k-1} I_0(t-k\tau) \end{aligned} \tag{5-1}$$

For pulsed lasers in the range of micro-second to nano-second, the energy density varies as a function of the square root of the pulse duration, and the laser damage threshold is given by Equation 5-2 [32,33]:

$$LDT(Y) = LDT(X)\sqrt{\frac{Y}{X}} \tag{5-2}$$

where *LDT* is the laser damage threshold, *X* is original pulse duration, and *Y* is the new pulse duration. Therefore, the fiber input end damage threshold is proportional to the square root of the laser pulse width.

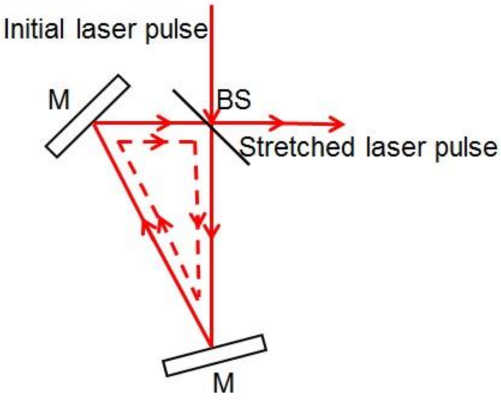

Figure 5-1. Schematic of laser pulse stretching system based on a triangular ring cavity. M: mirror, BS: beam splitter.

5.2.3 Experimental setup

The photoacoustic imaging experimental setup is shown in Figure 5-2. A Ti:sapphire laser (Symphotics TII, LS-2134) pumped with a Q-switched Nd:YAG laser (Symphotics TII, LS-2122) operated at a wavelength of 745 nm with a FWHM of 17 ns and a repetition rate of 15 Hz. The laser beam was expanded with a Galilean telescope and then reflected into cavity of the triangular ring pulse stretcher. The beam splitter had a reflectivity / transmission ratio of 40/60, and the ring cavity length was 4.5m. The energy throughput of the pulse stretcher was 92%. Most of the 8% energy loss resulted from the divergence of the laser beam, which expanded the beam size beyond that of the mirrors and beam splitter. The use of larger-size optical components will significantly decrease the loss. A 0.5 mm-diameter music wire, and tube of inner diameter 0.58 mm and outer diameter 0.97 mm filled with rat blood were used as targets to generate photoacoustic waves. Two sets of experiments were performed to compare photoacoustic measurement data and image quality obtained with the original and stretched laser pulses. In the photoacoustic measurement experiment, a broadband hydrophone (Force Institute, Copenhagen) with a flat frequency response from 1 to 10 MHz was used. Its output was amplified by a Panametrics receiver (Panametrics 5072PR) and sampled by a digital oscilloscope of 300 MHz bandwidth (Tektronix, TDS3032). The corresponding bandpass filters were applied in software to simulate the transducers. In the photoacoustic imaging experiment, three ultrasound transducers centered at 1.3 MHz (Vermon, France), 3.5 MHz (GE, Medical Systems), 6 MHz (W.L. Gore&Associates Inc) of 120%, 80%, 80% fractional bandwidth were used respectively. Both the wire and tube were imaged in the transverse directions. The receiving electronics consisted of 64 parallel pre-amplifiers of

20 dB gain and outputs of the pre-amplifiers were multiplexed to two parallel channels for further amplification, low pass filtering and analog-to-digital (A/D) conversion. The system was controlled with a custom C-language software on the host computer through the two digital I/O cards connected to the A/D. Delay and sum beamforming algorithm was used for photoacoustic image reconstruction.

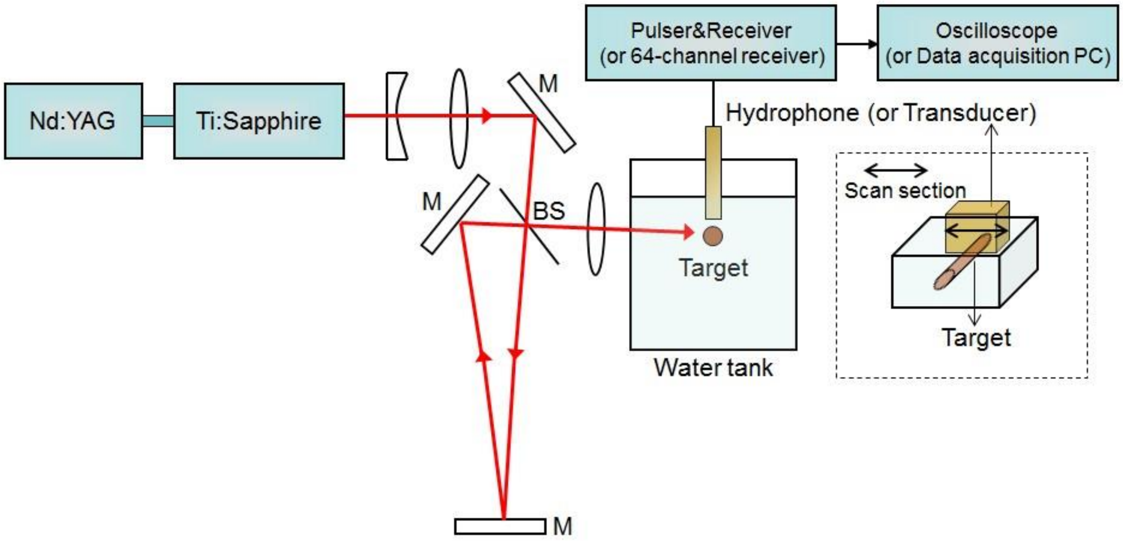
Pulser&Receiver
(or 64-channel receiver)
Oscilloscope
(or Data acquisition PC)
Nd:YAG
Ti:Sapphire
M
Hydrophone (or Transducer)
M
BS
Scan section
Target
Target
Water tank
M

Figure 5-2. Experimental setup of photoacoustic imaging using stretched laser pulse. M: mirror, BS: beam splitter.

5.2.4 Imaging quality comparison

To quantitatively compare the image quality using the original and stretched pulses, the image contrast and resolution were calculated from the target response. The beam line across the center of the target was extracted. The ratio of peak value and the averaged background value was used to estimate the contrast, and FWHM was used to estimate the temporal resolution.

5.3 Simulation and experimental results

5.3.1 Simulations

The photoacoustic spectrum is affected by using laser pulses of different widths and targets of different sizes. Figure 5-3 shows the FFT of photoacoustic signals obtained with FWHM of 6 ns and 50 ns laser pulses of both the same energy. Figure 5-3 (a) and 5-3 (b) show the results of using 0.25 mm and 2 mm diameter targets respectively. For the 0.25 mm-diameter target, the spectrum shifted to a lower frequency range and a small fraction of the amplitudes of both the lower and higher frequency components was lost as the pulse width increased. For the 2 mm-diameter target, the amplitudes of the lower frequency components were almost the same but that of the higher frequency components decreased a little as the pulse width increased. In general, the photoacoustic signal generated by the 6 ns laser pulse was higher than that generated by 50 ns laser pulse, which was due to the more efficient acoustic wave generation achieved by shorter pulses [34]. In addition, by comparing Figure 5-3 (a) with 5-3 (b), the main peak of the spectrum shifted to a lower frequency as the target size was increased.

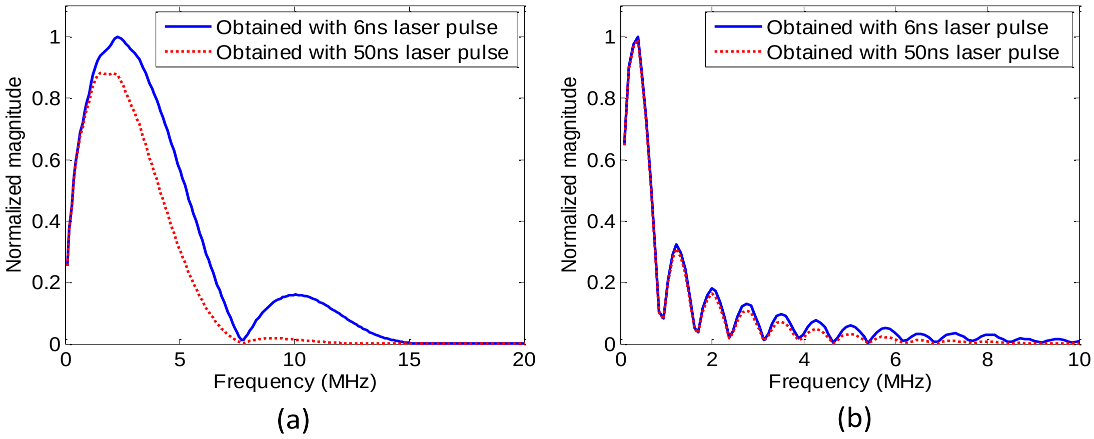

Figure 5-3. Frequency-domain photoacoustic signals obtained with 6 ns and 50 ns laser pulses. (a) 0.25 mm-diameter target, (b) 2 mm-diameter target.

To systematically study the pulse width effect, photoacoustic signals obtained with equal-energy pulse widths ranging from 6 ns to 50 ns were simulated using MATLAB k-Wave toolbox. In the simulations, different target sizes with diameters of 4 mm, 2 mm, 1 mm, 0.5 mm and 0.25 mm were used to generate photoacoustic signals. The photoacoustic signal was simulated by integrating the frequency domain signals that can be received by each ultrasound transducer. The results using the three transducers are shown in Figure 5-4 (a), 5-4 (b) and 5-4 (c) respectively. The left y-axis of each figure represents the photoacoustic signals, which are normalized to the photoacoustic signal obtained with the 6 ns laser pulse. The right y-axis represents the fiber damage threshold, which is normalized to the fiber damage threshold by using 6 ns laser pulse**.** If other conditions are fixed, the fiber damage threshold is proportional to the square root of the laser pulse width based on Equation 5-2. For all the three transducers, the photoacoustic signals decreased as the pulse width increased; at the same time, the fiber damage threshold increased. Compared to the 6 ns pulse, the photoacoustic signals obtained with the 50 ns pulse was more than 94%, 75%, 58% for the 1.3 MHz, 3.5 MHz, 6 MHz transducers respectively. Following this, the fiber damage threshold increased by 2.9-fold. In some cases, the laser pulse might not need to be stretched that much as from 6 ns to 50 ns, so that the photoacoustic signal was almost not affected. For example, if stretching the laser pulse from 6 ns to 14 ns, the photoacoustic signal of 0.5 mm-diameter target obtained by 1.3 MHz, 3.5 MHz, 6 MHz transducer was about 99.1%, 97.9%, 95.7% respectively after stretching the pulse, and as a reward, the fiber damage threshold was increased by 1.5-fold. These results are useful for designing a laser pulse stretcher in order to increase the fiber damage threshold to ensure that higher laser energy can be delivered to the imaged tissue by fibers. Figure 5-4 also shows that the photoacoustic signals were less sensitive to target size for the three types of transducers and the range of target sizes evaluated.

5.3.2 Experimental results

The triangular ring-cavity laser pulse stretching system stretched the initial 17 ns (FWHM) laser pulse to 27 ns and 37 ns laser pulses as shown in Figure 5-5. The peak intensity of the 27 ns and 37 ns laser pulse was reduced to about 58% and 42% of the initial 17 ns pulse, and the fiber damage threshold was increased by 1.3-fold and 1.5-fold respectively.

(a) **1.3MHz transducer**

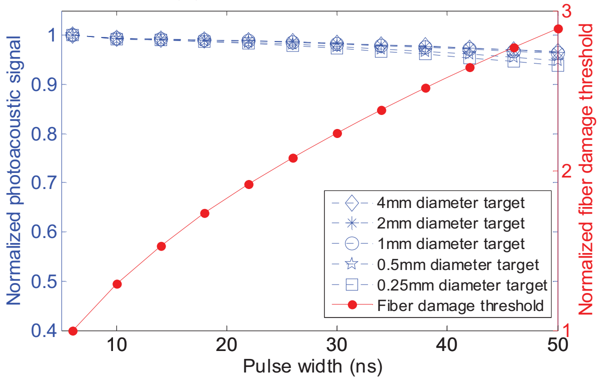

(b) **3.5MHz transducer**

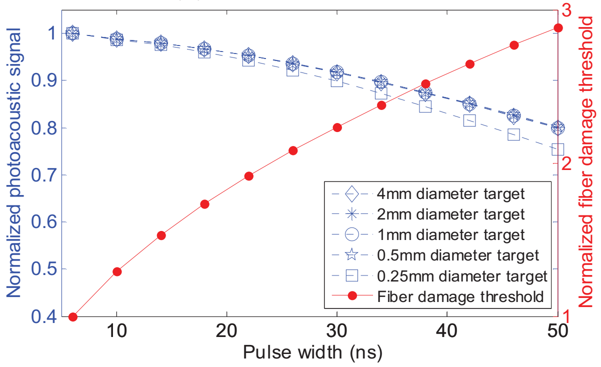

(c) **6MHz transducer**

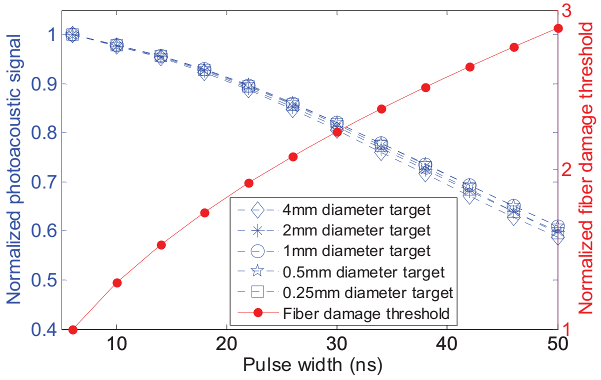

Figure 5-4. Simulations of normalized photoacoustic signal and normalized fiber damage threshold versus laser pulse width. The photoacoustic signal was obtained with (a) 1.3 MHz transducer, (b) 3.5 MHz transducer, (c) 6 MHz transducer.

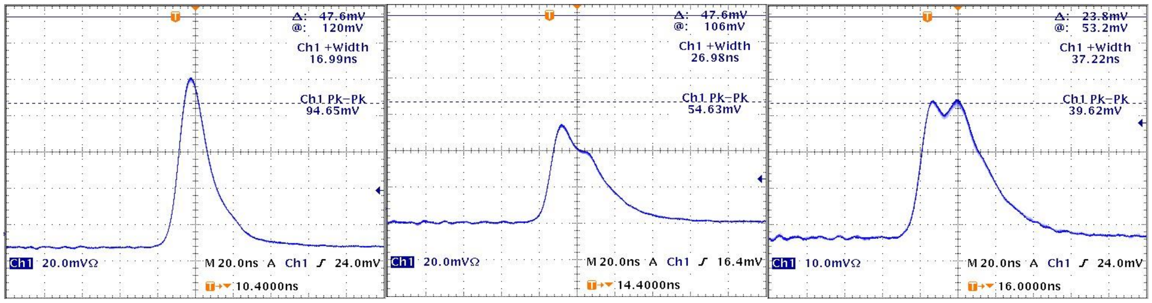

(a) (b) (c)

Figure 5-5. Profile of laser pulses. (a) Initial 17 ns laser pulse, (b) stretched 27 ns laser pulse, (c) stretched 37 ns laser pulse.

5.3.2.1 Experimental validations

The simulations were validated using a hydrophone. The photoacoustic signals of the 0.5 mm-diamter music wire obtained with pulse widths of 17 ns, 27 ns and 37 ns all having the same energy, and the aforementioned transducers are shown in Figure 5-6. The corresponding bandpass filters were applied to the photoacoustic signals received by hydrophone and averaged over four experimental data. The left y-axis of each figure corresponds to the normalized photoacoustic signals, and the right y-axis corresponds to the normalized fiber damage threshold. The experimental results show that using the 1.3 MHz transducer, the photoacoustic signals obtained with the 27 ns and 37 ns stretched pulse are about 96.7% (std 7.0%) and 95.8% (std 4.7%) respectively of the initial 17 ns laser pulse, and agree well with the simulation results of 99.2% and 97.9%. Again for the 3.5 MHz transducer, the photoacoustic signals obtained with those stretched pulses are about 97.6% (std 5.8%) and 90.6% (std 3.5%) of the initial 17ns laser pulse; this also agrees well with the simulation results of 96.0% and 90.7%. Finally, for the 6 MHz transducer, the photoacoustic signals obtained with the stretched pulses are about 95.5%

(std 7.2%) and 83.7% (std 8.8%) of the initial 17 ns laser pulse; this agrees well with the simulation results of 90.8% and 79.5%. At the same time, by stretching the laser pulse to 27 ns and 37 ns, the fiber damage threshold was increased by 1.3-fold and 1.5-fold, which is significant in delivering higher energy laser light to image deeply-seated targets. Both simulation and experimental results indicate that by stretching the laser pulse from 17 ns to 37 ns, the fiber damage threshold is improved without much loss of photoacoustic signal.

5.3.2.2 Imaging comparisons

The photoacoustic images of 0.5 mm-diameter music wire obtained with pulse widths of 17 ns and 37 ns having the same energy, and the aforementioned transducers are shown in Figure 5-7 (a) and 5-7 (b), 5-7 (c) and 5-7 (d), 5-7 (e) and 5-7 (f) respectively in log-scale. The dynamic range of the image was set to 30dB. The scan section of the transducer was placed perpendicular to the target during imaging. The image quality was not affected by stretching the pulse by visually comparing those images.

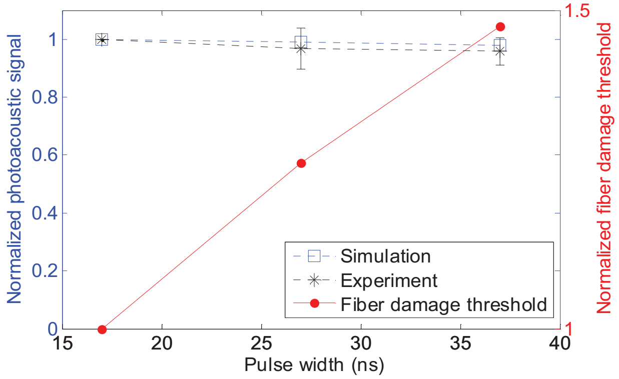
(a) **1.3MHz transducer**

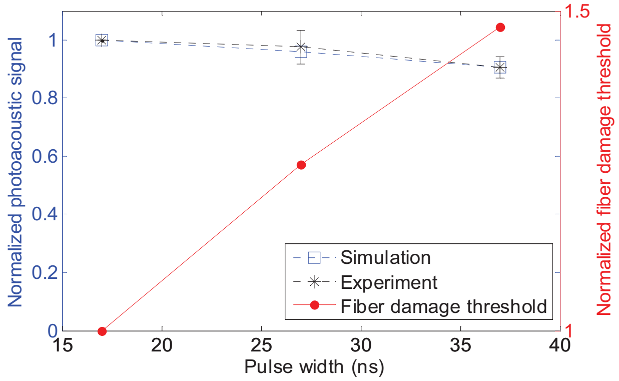
(b) **3.5MHz transducer**

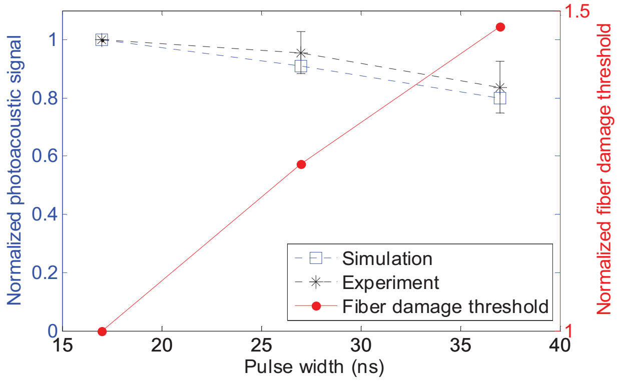
(c) **6MHz transducer**

Figure 5-6. Simulations and experimental results of normalized photoacoustic signal and normalized fiber damage threshold versus laser pulse width. The photoacoustic signal was obtained with (a) 1.3 MHz transducer, (b) 3.5 MHz transducer, (c) 6 MHz transducer.

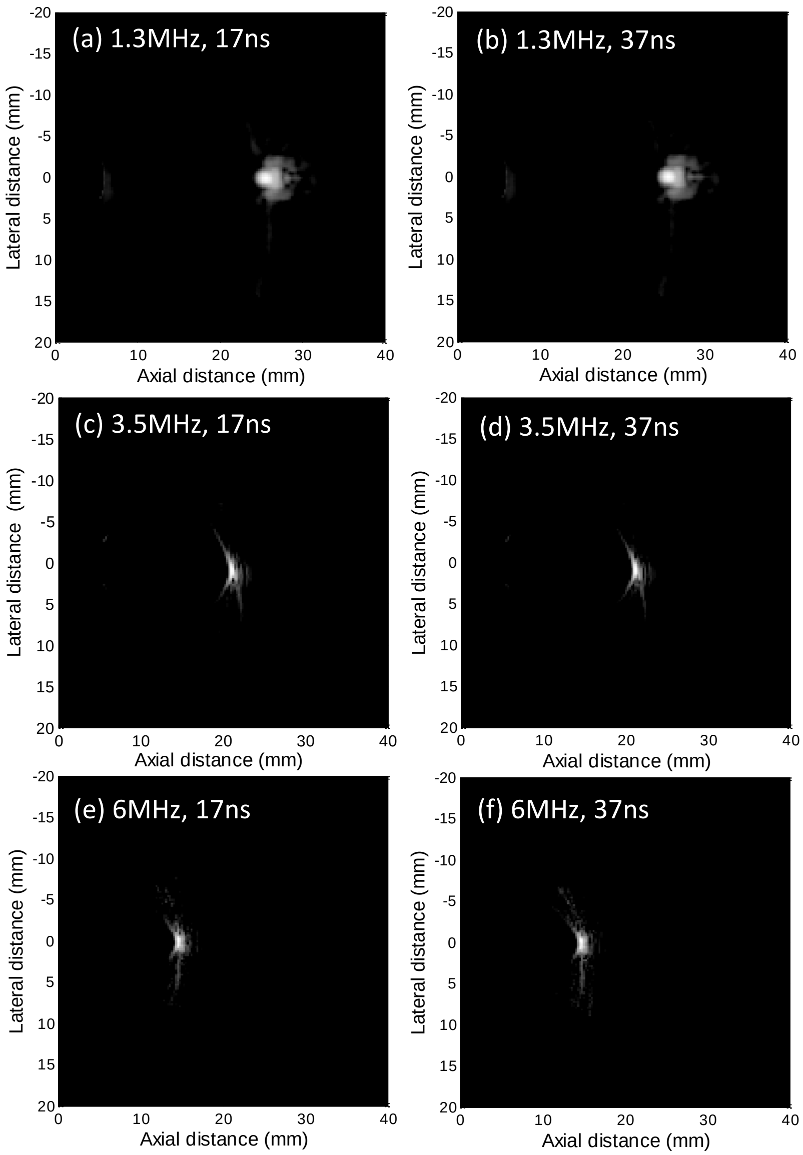
(a) 1.3MHz, 17ns
(b) 1.3MHz, 37ns
(c) 3.5MHz, 17ns
(d) 3.5MHz, 37ns
(e) 6MHz, 17ns
(f) 6MHz, 37ns
Lateral distance (mm)
Axial distance (mm)
-20
-15
-10
-5
0
5
10
15
20
0
10
20
30
40

Figure 5-7. Photoacoustic images of 0.5 mm-diameter music wire obtained with (a) 1.3 MHz transducer, 17 ns laser pulse; (b) 1.3 MHz transducer, same energy of stretched 37 ns laser pulse. (c) 3.5 MHz transducer, 17 ns laser pulse; (d) 3.5 MHz transducer, same energy of stretched 37ns laser pulse. (e) 6 MHz transducer, 17ns laser pulse; (f) 6 MHz transducer, same energy of stretched 37ns laser pulse.

The photoacoustic images of blood tube obtained with pulse widths of 17 ns and 37 ns having the same energy, and the aforementioned transducers are shown in Figure 5-8 (a) and 5-8 (b), 5-8 (c) and 5-8 (d), 5-8 (e) and 5-8 (f) respectively in log-scale. Similar as the images of music wire, the image quality of the blood tube was not affected by stretching the pulse by visually comparing those images. Note that the images of Figure 5-7 (c)-(d) and Figure 5-8 (c)-(d) were slightly defocused. This 3.5 MHz transducer was designed for cardiac imaging and had the acoustic lens of 7 cm elevation focal depth. However, the targets were located around 2 cm for comparison with the images obtained by 1.3 and 6 MHz linear arrays with the elevation focal depth fixed at 2 cm.

The image contrast and resolution were calculated to compare the image quality quantitatively. Figure 5-9 illustrates the contrast and resolution calculation. Figure 5-9 (a) shows the beam line across the center of the target image. The signal in the dash rectangular area was the background, and the contrast was estimated by calculating the ratio of the peak value and the averaged background value. Figure 5-9 (b) is the zoomed in portion of solid rectangular area in Figure 5-9 (a). The FWHM was calculated to estimate the temporal resolution. The quantitative comparison results are shown in Table 5-1. Three averages were done for each ratio. For both music wire and blood tube targets, the contrast and the resolution did not show much difference between 17 ns and 37 ns laser pulses.

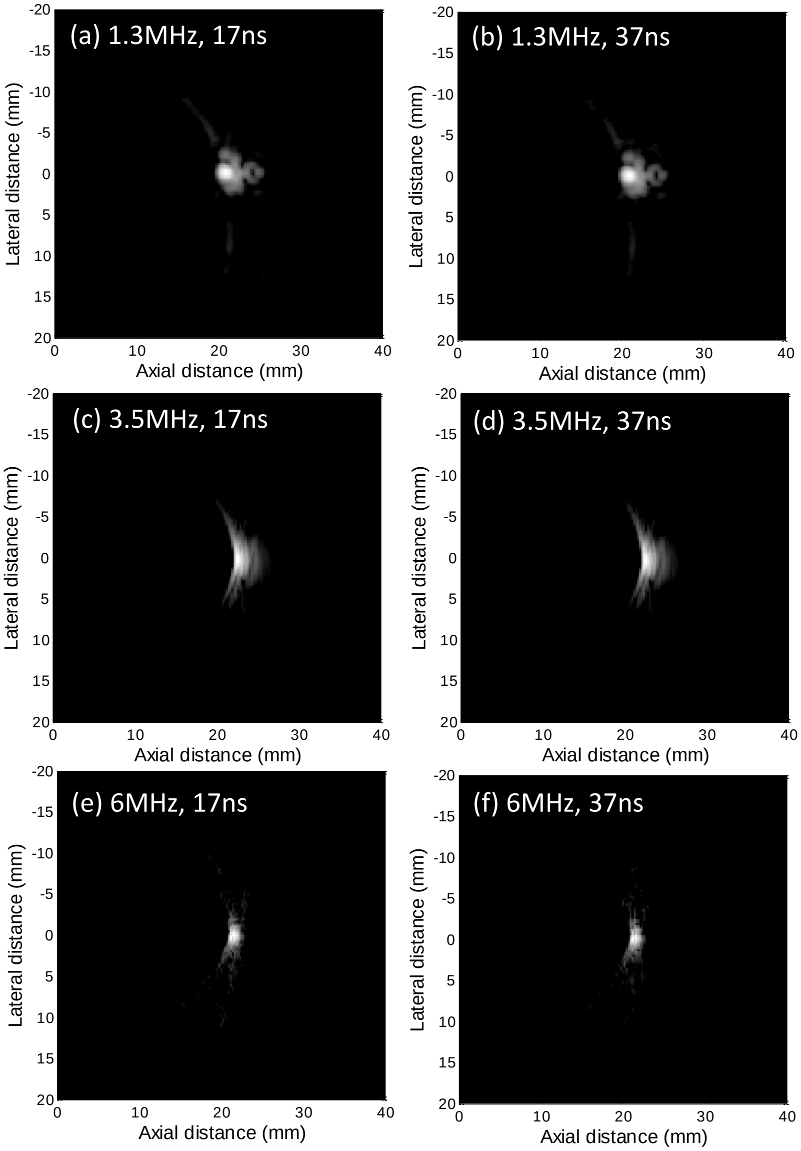
(a) 1.3MHz, 17ns
(b) 1.3MHz, 37ns
(c) 3.5MHz, 17ns
(d) 3.5MHz, 37ns
(e) 6MHz, 17ns
(f) 6MHz, 37ns
Lateral distance (mm)
-20
-15
-10
-5
0
5
10
15
20
Axial distance (mm)
0
10
20
30
40

Figure 5-8. Photoacoustic images of blood tube obtained with (a) 1.3 MHz transducer, 17 ns laser pulse; (b) 1.3 MHz transducer, same energy of stretched 37 ns laser pulse. (c) 3.5 MHz transducer, 17 ns laser pulse; (d) 3.5 MHz transducer, same energy of stretched 37 ns laser pulse. (e) 6 MHz transducer, 17 ns laser pulse; (f) 6 MHz transducer, same energy of stretched 37n s laser pulse.

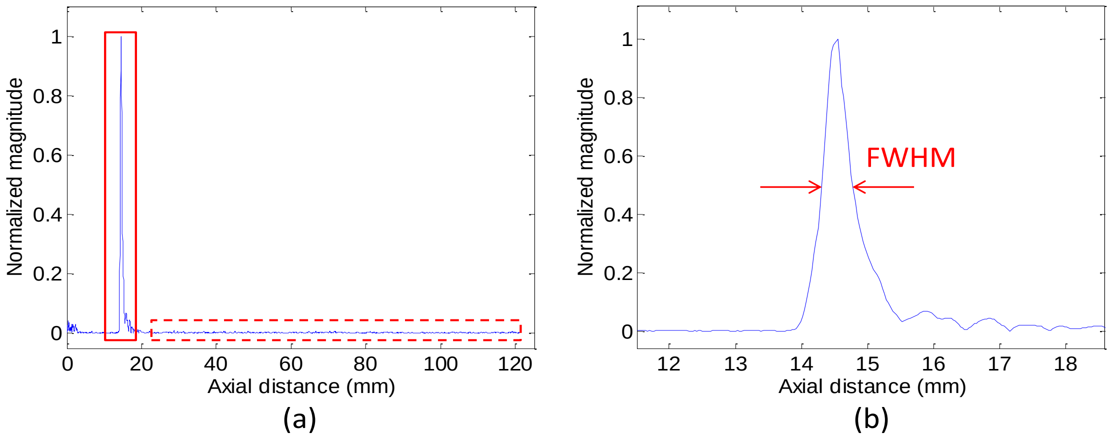

Figure 5-9. The beam line across the center of the target. (a) Illustration of contrast calculation. (b) Zoomed in of solid rectangular area in 5-9 (a) to illustrate resolution calculation.

By stretching the laser pulse from 17 ns to 37 ns, the fiber damage threshold increased by 1.5-fold. Therefore, the upper limit energy that can be delivered by the fiber also increased by 1.5-fold. If MPE is not exceeded, higher energy can be coupled into the fiber, so that higher energy can be delivered to the imaged tissue by stretching the laser pulse. Figure 5-10 shows the comparisons of music wire images using 17 ns pulse and 1.5-fold energy of stretched 37 ns pulse. Similar as the quantitative comparison in Table 5-1, Table 5-2 shows the contrast and resolution ratio of 1.5-fold energy of stretched 37 ns pulse and initial 17 ns pulse. In this case, the image contrast is improved after stretching the pulse.

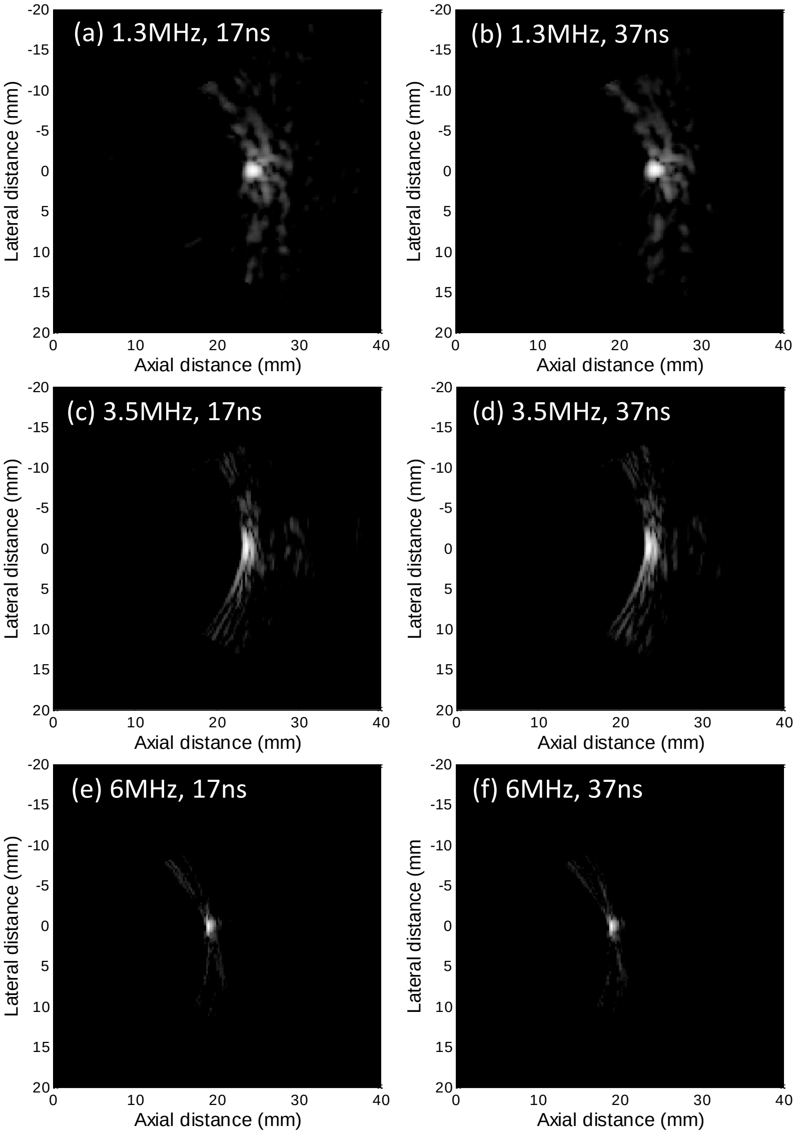
(a) 1.3MHz, 17ns
(b) 1.3MHz, 37ns
(c) 3.5MHz, 17ns
(d) 3.5MHz, 37ns
(e) 6MHz, 17ns
(f) 6MHz, 37ns
Lateral distance (mm)
Axial distance (mm)
-20
-15
-10
-5
0
5
10
15
20
0
10
20
30
40

Figure 5-10. Photoacoustic images of 0.5 mm-diameter music wire obtained with (a) 1.3 MHz transducer, 17 ns laser pulse; (b) 1.3 MHz transducer, 1.5-fold energy of stretched 37 ns laser pulse. (c) 3.5 MHz transducer, 17 ns laser pulse; (d) 3.5 MHz transducer, 1.5-fold energy of stretched 37 ns laser pulse. (e) 6 MHz transducer, 17 ns laser pulse; (f) 6 MHz transducer, 1.5-fold energy of stretched 37 ns laser pulse.

Table 5-1. Photoacoustic image quality comparison using same energy of 17 ns and 37 ns pulses. Contrast (resolution) ratio = Contrast (resolution) obtained with 37 ns laser pulse / 17 ns laser pulse. (a) Music wire comparison. (b) Blood tube comparison.

(a)

	Contrast ratio (Std)	**Resolution ratio (Std)**
1.3MHz transducer	0.976 (0.010)	0.987 (0.011)
3.5MHz transducer	0.929 (0.035)	1.076 (0.069)
6MHz transducer	0.892 (0.007)	0.979 (0.036)

(b)

	Contrast ratio (Std)	**Resolution ratio (Std)**
1.3MHz transducer	0.991 (0.005)	0.993 (0.012)
3.5MHz transducer	0.932 (0.025)	0.991 (0.032)
6MHz transducer	0.892 (0.026)	1.012 (0.020)

Table 5-2. Photoacoustic image quality comparison using 17 ns and 1.5-fold energy of 37 ns pulses.

	Contrast ratio (Std)	**Resolution ratio (Std)**
1.3MHz transducer	1.477 (0.067)	1.000 (0.020)
3.5MHz transducer	1.334 (0.033)	1.020 (0.057)
6MHz transducer	1.264 (0.030)	0.976 (0.041)

5.4 Discussion and summary

A series of simulations and experiments have been completed to investigate the laser pulse stretching effect on photoacoustic imaging. The results presented for the laser pulse width range and target size range show that by stretching the laser pulse, the image quality is not affected and the fiber damage threshold is increased. This helps protect the fiber input face during high-energy photoacoustic imaging of deeply-seated tissue. Provided the MPE is not exceeded, higher energy can be coupled into the fiber for delivery to the imaged tissue to improve the signal-to-noise ratio. In addition, some of the 8% energy loss during pulse stretching resulted from the divergence of the laser beam, which was not fit for our current mirror and beam-splitter size. If we use larger size of mirrors and beam splitter, this triangular ring-cavity laser pulse stretcher would have higher energy efficiency, and the only energy loss could come from the slight loss of mirrors and beam splitter. One other problem of the ring-cavity pulse stretching system right now is that it is bulky for clinical use as the cavity length used for the pulse stretching was 4.5 m. To solve this problem, we plan to use laser pulse stretcher made from fibers [35]. The laser beam was split to many parts, and then input into fibers with different lengths to induce optical delays, and the output laser light with different optical delays recombined together to generate a longer pulse with the same total energy.

The simulation and measurement reported in this paper have focused on the 6 ns-50 ns pulse width range and the 0.25 mm-4 mm target diameter range which is about ultrasound wavelength for typical 1 to 8 MHz transducers. In this range of target size, the stress confinement condition is stringently satisfied. The pulse stretching effect on the detected photoacoustic signals is less sensitive to target properties, including the size, the absorption and scattering properties. However, if the optical penetration depth in the target or the fully penetrated target size is smaller than the range studied, the photoacoustic signals will be affected more by stretching the laser pulse. The detected photoacoustic signals depend on the target sizes or optical penetration depth (whichever is smaller) and ultrasound transducer central frequencies.

In summary, we report a laser pulse stretching scheme for efficiently delivering laser energy to tissue while reducing the peak intensity for minimizing the fiber damage. To demonstrate the principle, we have compared photoacoustic signals and images obtained with 17 ns, and the stretched 27 ns, 37 ns laser pulses. The peak power of the stretched 37 ns pulse was reduced to 42% of the original pulse to significantly reduce the damage of the input fiber. Simulations and experimental results showed that the stretching technique increased the fiber damage threshold and the image quality was not affected.

References

1. T. Wang, P. Kumavor, and Q. Zhu, “Application of laser pulse stretching scheme for efficiently delivering laser energy in photoacoustic imaging,” J. Biomed. Opt. 17(6), 061218 (2012).
2. M. Xu and L. V. Wang, “Photoacoustic imaging in biomedicine,” Rev. Sci.Instrum. 77(4), 041101 (2006).
3. L. V. Wang, “Prospects of photoacoustic tomography,” Med. Phys. 35(12), 5758-5767 (2008).
4. J. Oh, M. Li, H. Zhang, K. Maslov, G. Stoica, and L. V. Wang, “Three-dimensional imaging of skin melanoma in vivo by dual-wavelength photoacoustic microscopy,” J. Biomed. Opt. 11(3), 34032 (2006).
5. J. Gamelin, A. Maurudis, A. Aguirre, F. Huang, P. Guo, L. V. Wang, and Q. Zhu, “A real-time photoacoustic tomography system for small animals,” Opt. Express 17(13), 10489-10498 (2009).
6. J. Gamelin, A. Aguirre, A. Maurudis, F. Huang, D. Castillo, L. V. Wang, and Q. Zhu, “Curved array photoacoustic tomographic system for small animal imaging,” J. Biomed. Opt. 13(2), 024007 (2008).

7. X. Wang, Y. Pang, G. Ku, X. Xie, G. Stoica, and L. V. Wang, “Noninvasive laser-induced photoacoustic tomography for structural and functional in vivo imaging of the brain,” Nature Biotechnol. 21(7), 803-806 (2003).
8. S. Manohar, A. Kharine, J. C. van Hespen, W. Steenbergen, and T. G. van Leeuwen, “The Twente Photoacoustic Mammoscope: system overview and performance,” Phys. Med. Biol. 50(11), 2543-2557 (2005).
9. A. Aguirre, Y. Ardeshirpour, M. M. Sanders, M. Brewer, and Q. Zhu, “Potential role of coregistered photoacoustic and ultrasound imaging in ovarian cancer detection and characterization,” Transl. Oncol. 4(1) 29-37 (2011).
10. P. D. Kumavor, U. Alqasemi, B. Tavakoli, H. Li, Y. Yang, X. Sun, E. Warych, and Q. Zhu, “Coregistered pulse-echo/photoacoustic transvaginal probe for real time imaging of ovarian tissue,” J. Biophotonics 6(6-7), 475-484 (2013).
11. B. Wang, J. L. Su, A. B. Karpiouk, K. V. Sokolov, R. W. Smalling, and S. Y. Emelianov, “Intravascular photoacoustic imaging,” IEEE J. Quantum Electron. 16(3), 588-599 (2010).
12. B. Wang, J. L. Su, J. Amirian, S. H. Litovsky, R. Smalling, and S. Emelianov, “Detection of lipid in atherosclerotic vessels using ultrasound-guided spectroscopic intravascular photoacoustic imaging, ” Opt. Express 18(5), 4889-4897 (2010).
13. J. Yang, K. Maslov, H. Yang, Q. Zhou, K. K. Shung, and L. V. Wang, “Photoacoustic endoscopy, ” Opt. Lett. 34(10), 1591-1593 (2009).
14. S. Seidel and G. Phillipps, “Pulse lengthening by intracavity stimulated Brillouin scattering in a Q-switched, phase-conjugated Nd:YAG laser oscillator,” Appl. Opt. 32(36), 7408-7417 (1993).
15. F. Beyrau, M.C. Weikl, T. Seeger, and A. Leipertz, “Application of an optical pulse stretcher to coherent anti-Stokes Raman spectroscopy,” Opt. Lett. 29(20), 2381-2383 (2004).
16. R. A. Robinson and I. K. Llev, “Design and optimization of a flexible high-peak-power laser-to-fiber coupled illumination system used in digital particle image velocimetry,” Rev. Sci. Instrum. 75(11), 4856-4862 (2004).
17. R. E. Kumon, C. X. Deng, and X. Wang, “Frequency-domain analysis of photoacoustic imaging data from prostate adenocarcinoma tumors in a murine model,” Ultrasound in Med. & Biol. 37(5), 834-839 (2011).
18. Laser Institute of America, “American National Standard for Safe Use of Lasers ANSI Z136. 1-2000,” American National Standard Institute (2000).
19. S. Pflüger, M. Sellhorst, V. Sturm, and R. Noll, “Fiber-optic transmission of stretched pulses from a Q-switched ruby laser,” Appl. Opt. 35(25), 5165-5169 (1996).
20. M. Amit, S. Lavi, G. Erez, and E. Miron, “Temporal and spatial properties of an oscillator-amplifier copper vapor laser,” Opt. Commun. 62(2), 110-114 (1987).
21. J. Kojima and Q. Nguyen, “Laser pulse-stretching with multiple optical ring cavities,” Appl. Opt. 41(30), 6360-6370 (2002).
22. A. Burkert, J. Bergmann, W. Triebel, and U. Natura, “Pulse stretcher with variable pulse length for excimer laser applications,” Rev. Sci. Instrum. 81(3), 033014 (2010).
23. R. Khare, P. K. Shukla, G. K. Mishra, C. Mukherjee, S. Talwar, V. K. Dubey, P. Saxena, and J. K. Mittal, “A novel confocal optical pulse stretcher for laser pulses,” Opt. Commun. 282(19), 3850-3853 (2009).

24. R. V. Lovberg, E. R. Wooding, and M. L. Yeoman, “Pulse stretching and shape control by compound feedback in a Q-switched ruby laser,” IEEE J. Quantum Electron. 11(1), 17-21 (1975).
25. L. Verluyten, S. Willocq, G. G. Harigel, J. K. Hawkins, W. M. Smart, W. A. Williams, M. W. Peters, and H. Akbari, “Laser pulse stretching via enhanced closed loop control with slow Q-switching,” Nucl. Instr. Meth. Phys. Res. A 292(2), 313-318 (1990).
26. P. Maine, D. Strickland, P. Bado, M. Pessot, and G. Mourou, “Generation of ultrahigh peak power pulses by chirped pulse amplification,” IEEE J. Quantum Electron. 24(2), 398-403 (1988).
27. J. Azuma, S. Asaka, T. Tsujibayashi, M. Itoh, M. Watanabe, O. Arimoto, S. Nakanishi, H. Itoh, and M. Kamada, “Optical detection system using time structure of UVSOR for combined laser-SR experiments,” Nucl. Instr. Meth. Phys. Res. A 467-468, 1455-1457 (2001).
28. A. K. Sharma, M. Raghuramaiah, K. K. Mishra, P. A. Naik, S. R. Kumbhare, and P. D. Gupta, “Characteristics of a stable, injection Q-switched Nd:phosphate glass regenerative amplifier for a chirped pulse amplification based Table Top Terawatt laser system,” Opt. Commun. 252(4-6), 369-380 (2005).
29. G. Bergamasco, P. Calvelli, W. Cecchetti, and P. Polloni, “Passive pulse stretching in an Nd:glass laser,” Opt. Quantum. Electron. 25(4), 271-273 (1993).
30. P. Dekker, J. M. Dawes, and J. A. Piper, “2.27-W Q-switched self-doubling Yb:YAB laser with controllable pulse length,” J. Opt. Soc. Am. B 22(2), 378-384 (2005).
31. B. E. Treeby and B. T. Cox, “k-Wave: Matlab toolbox for the simulation and reconstruction of photoacoustic wave fields,” J. Biomed. Opt. 15(2), 021314 (2010).
32. J. Bisson, Y. Feng, A. Shirakawa, H. Yoneda, J. Lu, H. Yagi, T. Yanagitani, and K. Ueda, “Laser damage threshold of ceramic YAG,” Jpn. J. Appl. Phys. 42(8B) 1025-1027 (2003).
33. H. Kessler, “Laser damage thresholds of optical coatings, UV-NIR,” Technical Reference. Document #20041108.
34. T. J. Allen, B. T. Cox, and P. C. Beard, “Generating photoacoustic signals using high-peak power pulsed laser diodes,” Proc. SPIE 5696, 233-242 (2005).
35. D. Hanna and J. W. Mitchell, “A laser pulse stretcher made from optical fibres,” Nucl. Instr. Meth. Phys. Res. A 324(1-2), 14-18 (1993).

6 Photoacoustic microscopy for ovarian cancer detection [1]

6.1 Introduction

Photoacoustic imaging has emerged as a promising biomedical imaging modality [2-4] and demonstrated great potential for imaging ovarian tissue [5-8]. Photoacoustic microscopy (PAM) in particular, is capable of mapping microvasculature networks in biological tissue and resolving blood vessels with much higher resolution than conventional photoacoustic images obtained with ultrasound array transducers [9-24]. Guo et al. performed the quantification of total hemoglobin concentration and hemoglobin oxygen saturation in a mouse using PAM [23]. Xie at al. studied the feasibility of PAM in differentiating malignant from benign bladder tissues [24]. In their study, the comparison of malignant and benign images was based on visual observations. Alqasemi et al. have introduced a recognition algorithm using a support vector machine for assisting ovarian cancer diagnosis, and they used features extracted from ultrasound and photoacoustic images obtained from array transducers of 5-6 MHz central frequency [7]. However, photoacoustic images obtained with conventional ultrasound array transducers in the central frequency range of 3-7 MHz have lower resolution in resolving microvasculature networks and distributions in ovarian tissue than that of PAM. In this chapter, we imaged *ex vivo* human ovaries with malignant and benign features using a newly developed OR-PAM system with lateral resolution of 6 μm. We extracted seven features from high resolution PAM images, and used a logistic model to classify the normal and malignant ovarian tissues. We also evaluated the diagnostic sensitivity, specificity, positive and negative predictive values (PPV, NPV) and the area under the receiver operating characteristic (ROC) curves (AUC). To the best of our knowledge, this study is the first one reporting quantitative analysis and feature extraction of PAM images for classifying normal and malignant ovarian tissues. Quantitative analysis of PAM images is extremely valuable in assisting physicians to characterize and diagnose normal and malignant processes.

6.2 Materials and methods

6.2.1 Ovary sample

Human ovaries were extracted from patients undergoing prophylactic oophorectomy at the University of Connecticut Health Center (UCHC). These patients were at risk for ovarian cancer or they had ovarian mass or pelvic mass suggesting malignancy. This study was approved by the Institutional Review Boards of UCHC, and informed consent was obtained from all patients. Ovaries were kept in the 0.9% wt/vol NaCl solution and imaged within 24 hours after oophorectomy. After PAM imaging, the ovaries were fixed in 10% formalin solution and returned to the Pathology Department for histological processing.

6.2.2 PAM system

The OR-PAM system configuration is shown in Figure 6-1. A Ti:sapphire laser pumped by a Q-switched Nd:YAG laser delivers 15 ns laser pulses at 745 nm with a repetition rate of 15 Hz. The laser beam is spatially filtered by an iris, and then focused on the ovary by using a 10X objective lens (NA = 0.25). Ultrasound (US) gel is used to couple the photoacoustic signal to a single element transducer (Echo, BI933) with a center frequency of 3.5 MHz and a bandwidth of 60%. The acquired photoacoustic signal is amplified by a Panametrics receiver and then sampled by a data acquisition (DAQ) PC. A 3D motor is used to scan the transducer together with the ovary to obtain PAM images, and the distance between the objective lens and the ovary can be adjusted to achieve optimal resolution.

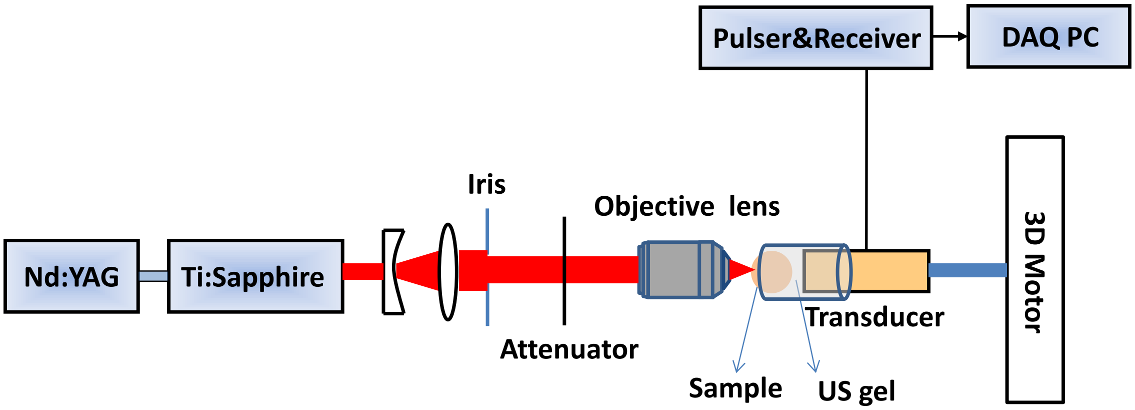
Pulser&Receiver
DAQ PC
3D Motor
Iris
Objective lens
Nd:YAG
Ti:Sapphire
Transducer
Attenuator
Sample
US gel

Figure 6-1. Configuration of the OR-PAM system.

6.2.3 Feature extraction

Several features were quantitatively extracted from the PAM images to classify normal and malignant ovaries, based on the observed differences between the PAM images of normal and malignant ovarian tissues in terms of microvasculature features and distributions. For example, the photoacoustic signal distribution is more scattered and diffuse in malignant cases, whereas the distribution is more clustered and the microvasculature networks are more clearly recognized in normal cases. These results suggest that the spatial frequency components, and the spatial spread of the PAM images are important. This observation also suggests that the statistical properties of the PAM images are of great importance to account for the photoacoustic signal fluctuation. In Reference 7, both statistical mean and variance were used as features to characterize normal and malignant ovarian tissues. However, the difference of statistical variance between normal and malignant PAM images was not significant ($p = 0.618$), and the diagnostic results based on PAM images were getting worse by adding this feature. Therefore, the statistical variance was not used in this study. Overall, seven parameters were extracted from PAM images: low frequency components, high frequency components, Gaussian fitting standard deviation (SD) of the mean Radon transform, Gaussian fitting error of the mean Radon transform, statistical mean, Gamma distribution mean and variance. Similar to the method used to extract features from B-scan ultrasound and photoacoustic images in Reference 7, all the 1.5 mm x 1.5 mm PAM images were normalized to their own maximum. The low frequency and high frequency components were calculated by selecting a low-pass window of the 2-D fast Fourier transform (FFT) with half of the sampling frequency. The average absolute value within that window was considered as low frequency component, while the average absolute value outside that window was considered as high frequency component. The average Radon transform from 0 degree to 90 degree was computed, and then fit to a Gaussian distribution. The Gaussian fitting SD was used to describe the spatial spread of the images, and the fitting error was used to describe the uniformity of the tissue absorption. The statistical properties were studied by calculating the statistical mean of the images. In addition, Gamma distribution mean and variance were calculated to account for those images that were not symmetrically distributed.

6.2.4 Logistic model

Logistic regression belongs to the class of generalized linear model (GLM) based on the exponential distribution family. It is a statistical model that can describe the relationship of several predictor variables to a dichotomous response variable (0 or 1). The logistic model was used to classify normal and malignant ovarian tissues. The seven parameters extracted from PAM images were used as predictor variables, and actual diagnosis results were used as the response variable (1 represents malignant and 0 represents normal). The MATLAB GLMFIT function was used to estimate the coefficients of the linear model, and then those coefficients were applied to the MATLAB GLMVAL function to calculate the responses. The quality of the logistic model was evaluated using ROC curve and AUC.

6.3 Results and discussion

6.3.1 Lateral resolution test

The lateral resolution of the PAM system was tested by imaging a 7 µm diameter carbon fiber. Figure 6-2 (a) shows the PAM maximum amplitude projection (MAP) image, and Figure 6-2 (b) shows normalized cross-sectional profile of the carbon fiber along the dotted line in Figure 6-2 (a). The full width at half maximum (FWHM) was estimated to be 13 µm. The subtraction value of FWHM and the carbon fiber diameter was used to estimate the lateral resolution of the system [13]. Therefore, the lateral resolution of the PAM system is ~6 µm. The axial resolution is ~360 µm, which is limited by the bandwidth of the transducer. The imaging quality of the PAM system was tested by imaging a mouse ear, as shown in Figure 6-3.

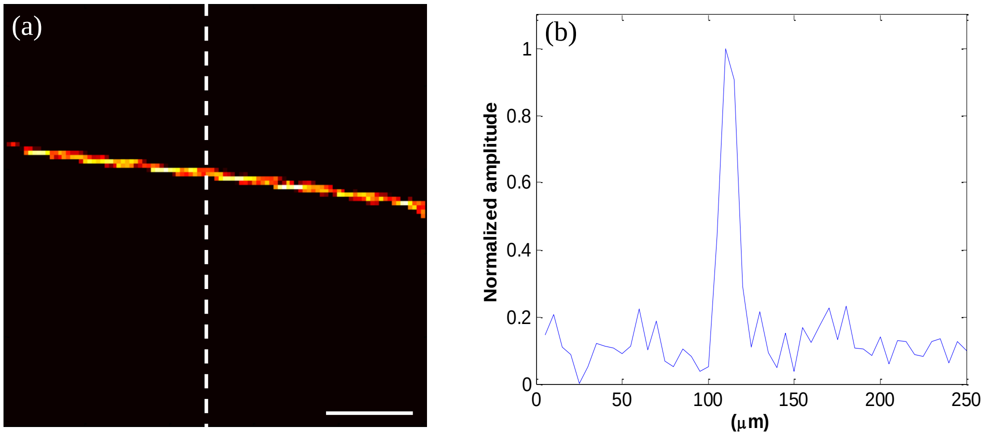

Figure 6-2. (a) PAM MAP image of a 7 µm carbon fiber, scale bar: 50 µm; (b) normalized cross-sectional profile of the carbon fiber along the dotted line in (a).

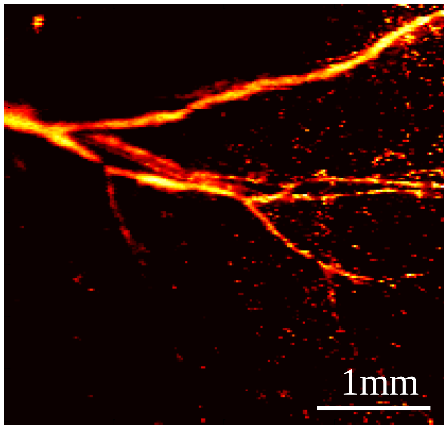

Figure 6-3. PAM MAP image of a mouse ear.

6.3.2 Ovarian tissue characterization

Some PAM images of normal and malignant ovarian tissues are presented in Figure 6-4 (a) and 6-4 (b), respectively. As shown by the MAP images, PAM was capable of imaging detailed microvasculature maps in ovarian tissue with much higher resolution than that of conventional photoacoustic images obtained with ultrasound array transducers [6-8]. In the normal ovarian tissue, the microvessel network consists of a larger vessel and several branching small vessels. The network shows more regular shape and better continuity, and these vessels are well organized. However, in the malignant ovarian tissue, the photoacoustic imaging features are diffuse and scattered which are likely caused by the extensive angiogenesis associated with malignancy of the ovary. The corresponding histology images of 6-4 (a) and 6-4 (b) are shown in Figure 6-4 (c) and 6-4 (d), respectively. The PAM images of both the normal and malignant ovaries match the histology. Based on the histology, the blood vessels in normal ovarian tissue form structured microvasculature networks, from large vessels to smaller ones, which are different from the scattered distributions seen in malignant ovary. For the malignant case, PAM image shows more blood vessels than histology image. The reason is that the PAM image is the maximum amplitude projection from multiple depths, while the histology image shows only one of the projected planes at a certain depth.

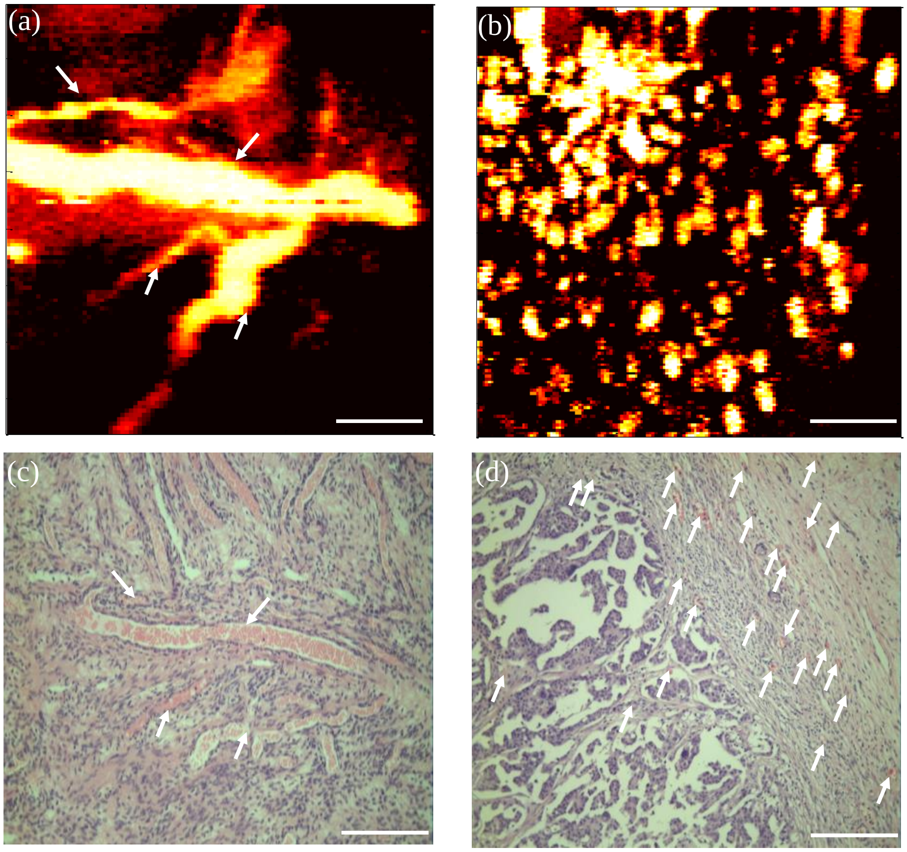

Figure 6-4. PAM images of (a) normal ovarian tissue and (b) malignant ovarian tissue; (c) H&E corresponding to (a); (d) H&E corresponding to (b); scale bar: 300 µm; arrows: blood vessels.

Figure 6-5 shows an example of mean Radon transform and Gaussian fitting curves. Figure 6-5 (a) shows a Radon transform of Figure 6-4 (a), and Figure 6-5 (b) is the Radon transform of Figure 6-4 (b). The Gaussian fitting error of the malignant example shown in Figure 6-5 (b) is larger than that of the normal one shown in Figure 6-5 (a).

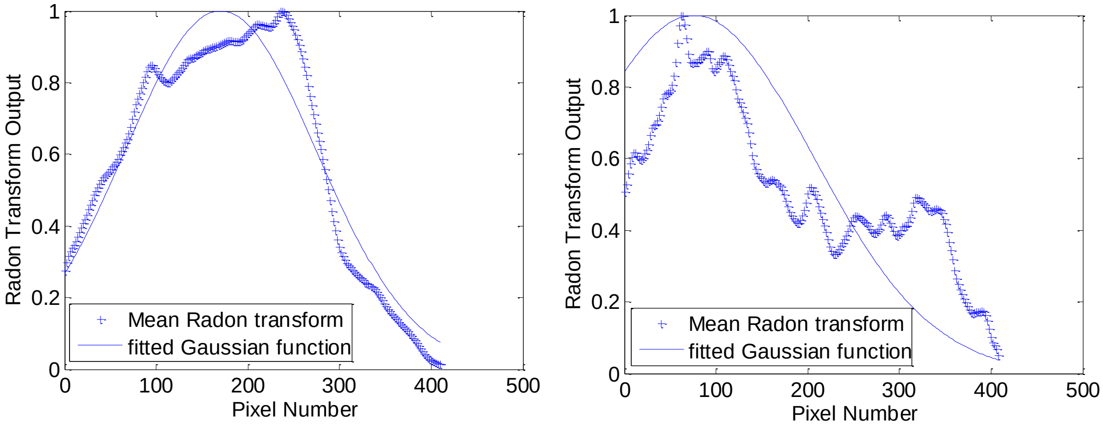

(a)

(b)

Figure 6-5. (a) Mean Radon transform and Gaussian fitting of Figure 6-4 (a), fitting SD: 74, fitting error: 1.5; (b) mean Radon transform and Gaussian fitting of Figure 6-4 (b), fitting SD: 91, fitting error: 8.3.

In order to investigate the differences of morphological features and statistical properties between normal and malignant ovarian tissues, we quantitatively extracted above-mentioned seven parameters from PAM images. 106 images (70 normal and 36 malignant) from 18 human ovaries (12 normal and 6 malignant) were acquired *ex vivo*. Figure 6-6 shows the boxplots and p values of seven parameters of normal and malignant ovary groups. To provide readers with statistical performance of these parameters, data from both training and testing sets were used in these plots. The differences of some parameters were highly statistically significant between normal and malignant groups. Note that for Gaussian fitting SD, the normal group had higher value than the malignant group, and the standard deviations of both normal and malignant groups were large.

Perhaps this was due to the diverse normal samples, for the normal group, the range of patient age was 43-77; for the malignant group, the range of patient age was 58-71. The seven parameters were used as predictor variables of the logistic model to classify normal and malignant ovaries. We separated all images into two groups, 57 images (38 normal and 19 malignant) were used as a training set to train the logistic classifier, and 49 images (32 normal and 17 malignant) were tested using our trained logistic prediction model. Figure 6-7 shows the ROC curves and AUC of training and testing set. For the training set, we could achieve 92.1% specificity, 89.5% sensitivity, 85.0% PPV, 94.6% NPV, and AUC (95% confidence interval) equals to 0.940 (0.869-1); for the testing set, we could achieve 81.3% specificity, 88.2% sensitivity, 71.4% PPV, 92.9% NPV, and AUC (95% confidence interval) equals to 0.886 (0.792-0.980).

The training and testing results are based on a limited sample pool, so more data will be acquired to validate these initial results. As a preliminary study, all ovarian tissue imaging was conducted *ex vivo*. For translating this technique from bench to bedside, a PAM system with a fiber catheter will replace free-space imaging for *in vivo* evaluation of ovarian tissue. In addition, the data acquisition speed of the current system is limited by the laser repetition rate of 15 Hz; by using a laser-diode based PAM system, the data acquisition speed can be increased by modulating the laser diode to ~kHz or even to ~MHz level.

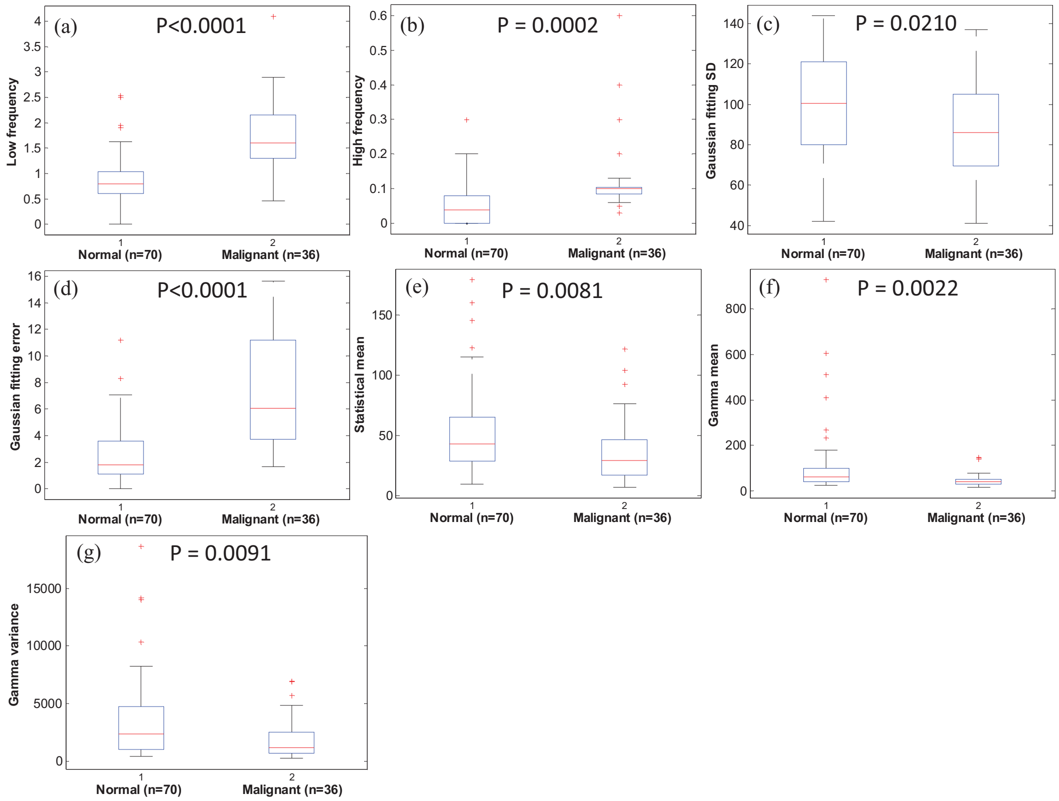

Figure 6-6. Boxplots of (a) low frequency; (b) high frequency; (c) Gaussian fitting SD; (d) Gaussian fitting error; (e) statistical mean; (f) Gamma mean; (g) Gamma variance.

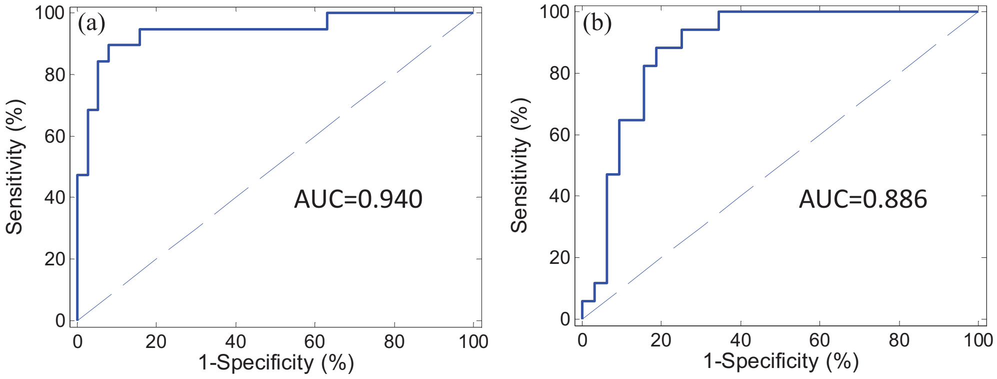

Figure 6-7. ROC curves of (a) training set; (b) testing set.

6.4 Photoacoustic microscopy with a laser diode excitation

The light source of the PAM system described in Section 6.2.2 is a Ti:sapphire laser pumped by a Q-switched Nd:YAG laser. The popularity of the PAM system is limited by the size and the cost of the solid-state laser source. A new PAM system based on a laser diode excitation is developed. The compact and low cost of the laser-diode-based PAM system would promote the potential clinical applications. The laser-diode PAM system is shown in Figure 6-8. The basic system configuration is similar to PAM system using Ti:Sapphire laser excitation. A pulsed laser diode (Laser Components) with wavelength of 905nm and output peak power of 130 W is used as an excitation source. The pulse repetition rate is 1 KHz, and the pulse width is 124 ns, as shown in Figure 6-9. The laser beam is collimated using a collimation tube (Thorlabs), and then focused on the imaged sample by using a 60X objective lens (NA = 0.7).

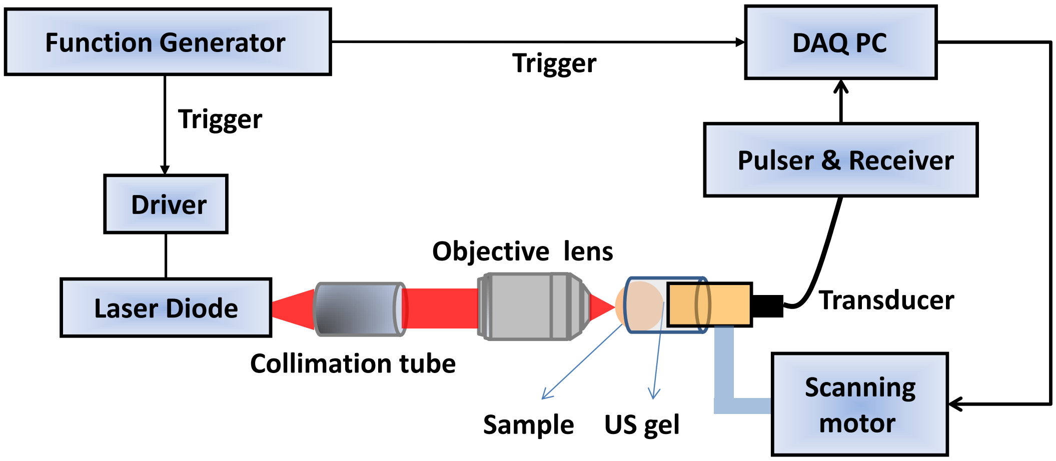
Function Generator
Trigger
DAQ PC
Trigger
Pulser & Receiver
Driver
Objective lens
Laser Diode
Transducer
Collimation tube
Scanning motor
Sample
US gel

Figure 6-8. Configuration of the laser-diode PAM system.

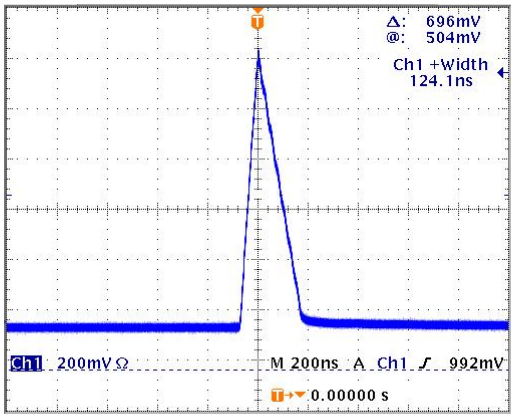

Figure 6-9. Profile of the diode laser; the pulse width is 124 ns.

The black-thread mesh was imaged using this newly-developed laser-diode PAM system. The MAP image of the thread mesh is shown in Figure 6-10. The carbon fiber and mouse ear will be imaged to further test this new system performance, and then the ovarian tissue will be imaged and characterized. The size and the cost of the laser-diode PAM system is significantly reduced compared with the solid-state-laser PAM system.

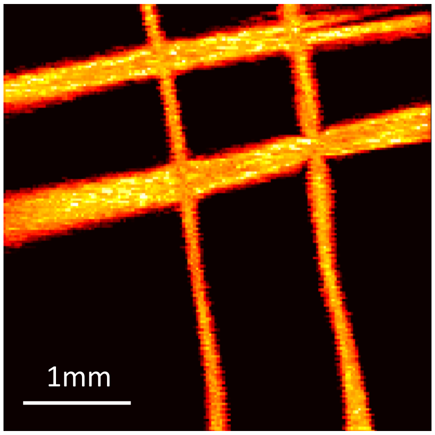

Figure 6-10. MAP image of black-thread mesh obtained by laser-diode PAM.

6.5 Summary

In this chapter, *ex vivo* ovarian tissue was imaged by using an OR-PAM system, and quantitative analysis was performed by extracting features from PAM images. The initial results have demonstrated that PAM was capable of imaging microvasculature maps in ovarian tissue. By utilizing a seven-parameter logistic model to classify PAM images of normal and malignant ovaries, we could achieve 92.1% specificity and 89.5% sensitivity in the training set, and 81.3% specificity and 88.2% sensitivity in the testing set. Meanwhile, a novel low-cost and compact PAM system based on laser-diode excitation is developed. The high resolution microvasculature network features extracted from PAM images could be extremely valuable in assisting and guiding surgeons for *in vivo* evaluation of ovarian tissue during minimally invasive surgery.

References

1. T. Wang, Y. Yang, U. Alqasemi, P. Kumavor, X. Wang, M. Sanders, M. Brewer, and Q. Zhu, “Characterization of ovarian tissue based on quantitative analysis of photoacoustic microscopy images,” Biomed. Opt. Express 4(12), 2763-2768 (2013).
2. M. Xu and L. V. Wang, “Photoacoustic imaging in biomedicine,” Rev. Sci. Instrum, 77(4), 041101 (2006).
3. L. V. Wang, “Prospects of photoacoustic tomography,” Med. Phys. 35(12), 5758-5767 (2008).
4. T. Wang, P. Kumavor, and Q. Zhu, “Application of laser pulse stretching scheme for efficiently delivering laser energy in photoacoustic imaging,” J. Biomed. Opt. 17(6), 061218 (2012).
5. A. Aguirre, P. Guo, J. Gamelin, S. Yan, M. M. Sanders, M. Brewer, and Q. Zhu, “Co-registered three-dimensional ultrasound and photoacoustic imaging system for ovarian tissue characterization,” J. Biomed. Opt. 14(5), 054014 (2009).
6. A. Aguirre, Y. Ardeshirpour, M. M. Sanders, M. Brewer, and Q. Zhu, “Potential role of coregistered photoacoustic and ultrasound imaging in ovarian cancer detection and characterization,” Transl. Oncol. 4(1) 29-37 (2011).

7. U. Alqasemi, P. Kumavor, A. Aguirre, and Q. Zhu, “Recognition algorithm for assisting ovarian cancer diagnosis from coregistered ultrasound and photoacoustic images: *ex vivo* study,” J. Biomed. Opt. 17(12), 126003 (2012).
8. P. Kumavor, U. Alqasemi, B. Tavakoli, H. Li, Y. Yang, X. Sun, Ed. Warych, and Q. Zhu, “Co-registered pulse-echo/photoacoustic transvaginal probe for real time imaging of ovarian tissue,” J. Biophotonics, 1-10, (2013).
9. K. Maslov, G. Stoica, and L. V. Wang, “*In vivo* dark-field reflection-mode photoacoustic microscopy,” Opt. Lett. 30(6), 625-627 (2005).
10. L. V. Wang and S. Hu, “Photoacoustic tomography: in vivo imaging from organelles to organs,” Science 335, 1458-1462 (2012).
11. J. Yao and L. V. Wang, “Photoacoustic microscopy,” Laser Photon Rev. 7(5), 758-778 (2013).
12. H. F. Zhang, K. Maslov, G. Stoica, and L.V. Wang., “Functional photoacoustic microscopy for high-resolution and noninvasive *in vivo* imaging,” Nat. Biotechnol. 24(7), 848-851 (2006).
13. K. Maslov, H. F. Zhang, S. Hu, and L. V. Wang, “Optical-resolution photoacoustic microscopy for *in vivo* imaging of single capillaries,” Opt. Lett. 33(9), 929-931 (2008).
14. R. J. Zemp, L. Song, R. Bitton, K. K. Shung, and L.V. Wang, “*In vivo* realtime photoacoustic microscopy with a 30-MHz ultrasound array transducer,” Opt. Express 16(11), 7915-7928 (2008).
15. L. V. Wang, “Multiscale photoacoustic microscopy and computed tomography,” Nat. Photon. 3(9), 503-509 (2009).
16. Z. Xie, S. Jiao, H. F. Zhang, and C. A. Puliafito, “Laser-scanning optical-resolution photoacoustic microscopy”, Opt. Lett. 34 (12), 1771-1773 (2009).
17. S. Hu, P. Yan, K. Maslov, J. Lee, and L. V. Wang, “Intravital imaging of amyloid plaques in a transgenic mouse model using optical-resolution photoacoustic microscopy,” Opt. Lett. 34(24), 3899-3901 (2009).
18. B. Rao, L. Li, K. Maslov, and L. V. Wang, “Hybrid-scanning optical-resolution photoacoustic microscopy for *in vivo* vasculature imaging,” Opt. Lett. 35(10), 1521-1523 (2010).
19. C. Zhang, K. Maslov, and L. V. Wang, “Subwavelength-resolution label-free photoacoustic microscopy of optical absorption *in vivo*,” Opt. Lett. 35(19), 3195-3197 (2010).
20. S. Hu, K. Maslov, and L. V. Wang, “Second-generation optical-resolution photoacoustic microscopy with improved sensitivity and speed,” Opt. Lett. 36(7), 1134-1136 (2011).
21. C. Zhang, K. Maslov, S. Hu, R. Chen, Q. Zhou, K. K. Shung, and L. V. Wang, “Reflection-mode submicron-resolution *in vivo* photoacoustic microscopy,” J. Biomed. Opt. 17(2), 020501 (2012).
22. L. Zeng, G. Liu, D.Yang, and X. Ji, “Portable optical-resolution photoacoustic microscopy with a pulsed laser diode excitation,” Appl. Phys. Lett. 102, 053704 (2013).
23. Z. Guo, C. Favazza, A. Garcia-Uribe, and L. V. Wang, “Quantitative photoacoustic microscopy of optical absorption coefficients from acoustic spectra in the optical diffusive regime,” J. Biomed. Opt. 17(6), 066011 (2012).

24. Z. Xie, W. Roberts, P. Carson, X. Liu, C. Tao, and X. Wang, “Evaluation of bladder microvasculature with high-resolution photoacoustic imaging,” Opt. Lett. 36(24), 4815-4817 (2011).

7 Conclusions and future work

In this dissertation, optical and photoacoustic imaging were investigated for ovarian cancer detection and characterization. Polarization-sensitive optical coherence tomography (PS-OCT) and photoacoustic microscopy (PAM) systems were developed. Tissue-related features were quantitatively extracted from PS-OCT and PAM images, and applied to a logistic prediction model for ovarian tissue diagnosis.

In the first study, optical scattering coefficient was quantitatively estimated by fitting conventional OCT signal to a single scattering model; 86% sensitivity and 100% specificity were achieved. Phase retardation was calculated from PS-OCT phase retardation image; 43% sensitivity and 100% specificity were achieved. Combining optical scattering coefficient and phase retardation for each ovary, a superior sensitivity of 100% and a specificity of 100% were achieved. Collagen content as assessed by Sirius Red staining correlates strongly with optical scattering coefficient and phase retardation.

In the second study, the phase retardation rate quantitatively extracted from PS-OCT has significantly improved the ovarian cancer diagnosis when it was used together with optical scattering coefficient and phase retardation. By using a new three-parameter logistic prediction model, we achieved 100% sensitivity and specificity in the training group; 100% sensitivity and 83.3% specificity in the testing group. The results demonstrated that the three-parameter prediction model based on PS-OCT could be a powerful tool to characterize ovarian tissue. A more compact PS-OCT system based on polarization-maintaining fiber was built.

In the third study, we designed a laser-pulse stretching scheme for efficiently delivering laser energy to tissue while reducing the peak intensity for minimizing the fiber damage in photoacoustic imaging. To demonstrate the principle, we compared photoacoustic signals and images obtained with 17 ns, and the stretched 27 ns and 37 ns laser pulses. The peak power of the stretched 37 ns pulse was reduced to 42% of the original pulse to significantly reduce the damage of the input fiber. Simulations and experimental results showed that the stretching technique increased the fiber damage threshold without affecting the image quality. On the other hand, considering the increased fiber damage threshold, higher energy can be coupled into fiber and delivered to the imaged tissue to improve the signal-to-noise ratio.

In the last study, ovarian tissue with malignant and benign features was imaged by using an optical-resolution PAM system, and quantitative analysis was performed by extracting features from PAM images. The results have demonstrated that PAM was capable of imaging microvasculature maps in ovarian tissue. By utilizing a seven-parameter logistic model to classify PAM images of normal and malignant ovaries, a sensitivity of 89.5% and a specificity of 92.1% were achieved in the training set; a sensitivity of 88.2% and a specificity of 81.3% were achieved in the testing set. Meanwhile, a compact and low-cost PAM system with laser diode excitation is built and tested. The high resolution microvasculature network features extracted from PAM images could be extremely valuable in assisting and guiding surgeons for characterizing ovarian tissue.

OCT and photoacoustic imaging have demonstrated great potential for ovarian cancer detection. Future efforts will be devoted to developing catheter-based probes for PS-OCT and PAM for *in vivo* inspection of ovaries during minimally invasive surgery. In addition, a multi-modality imaging system combining PS-OCT and PAM is under construction. Given that the promising diagnosis results achieved by using PS-OCT or PAM individually, a combined PS-OCT and PAM could provide more information, and further improve the sensitivity and specificity for ovarian cancer diagnosis.

List of publications

Peer-reviewed journal papers

1. **T. Wang,** M. Brewer, and Q. Zhu, "An overview of optical coherence tomography for ovarian tissue imaging and characterization," WIREs Nanomedicine & Nanobiotechnology (Submitted).
2. H. Salehi, P. Kumavor, U. Alqasemi, H. Li, **T. Wang,** and Q. Zhu, "Design of optimal light delivery system for co-registered transvaginal ultrasound and photoacoustic imaging of ovarian tissue," J. Biomed. Opt. (Under review).
3. **T. Wang,** Y. Yang, and Q. Zhu, "A three-parameter logistic model to characterize ovarian tissue using polarization-sensitive optical coherence tomography," Biomed. Opt. Express 4(5), 772-777 (2013).
4. **T. Wang,** Y. Yang, U. Alqasemi, P. Kumavor, X. Wang, M. Sanders, M. Brewer, and Q. Zhu, "Characterization of ovarian tissue based on quantitative analysis of photoacoustic microscopy images," Biomed. Opt. Express 4(12), 2763-2768 (2013).
5. Y. Xu, S. Zanganeh, I. Mohammad, A. Aguirre, **T. Wang,** Y. Yang, L. Kuhn, M. B. Smith, and Q. Zhu, "Targeting tumor hypoxia with 2-nitroimidazole-ICG dye conjugates," J. Biomed. Opt. 18(6), 066009 (2013).
6. **T. Wang,** P. D. Kumavor, and Q. Zhu, "Application of laser pulse stretching scheme for efficiently delivering laser energy in photoacoustic imaging," J. Biomed. Opt. 17(6), 061218 (2012).
7. Y. Yang*, **T. Wang*,** X. Wang, M. Sanders, M. Brewer, and Q. Zhu, "Quantitative analysis of estimated scattering coefficient and phase retardation for ovarian tissue

characterization," Biomed. Opt. Express **3**(7), 1548-1556 (2012). **(*The first two authors contributed equally to this work.)**

8. Y. Yang, **T. Wang,** M. Brewer, and Q. Zhu, "Quantitative analysis of angle-resolved scattering properties of ovarian tissue using optical coherence tomography," J. Biomed. Opt. 17(9), 090503 (2012).
9. Y. Yang, **T. Wang,** N. C. Biswal, X. Wang, M. Sanders, M. Brewer, and Q. Zhu, "Optical scattering coefficient estimated by optical coherence tomography correlates with collagen content in ovarian tissue," J. Biomed. Opt. 16(9), 090504 (2011).
10. Y. Yang, N. C. Biswal, **T. Wang,** P. D. Kumavor, M. Karimeddini, J. Vento, M. Sanders, M. Brewer, and Q. Zhu, "Potential role of a hybrid intraoperative probe based on OCT and positron detection for ovarian cancer detection and characterization," Biomed. Opt. Express 2(7), 1918-1930 (2011).
11. Y. Yang, X. Li, **T. Wang,** P. D. Kumavor, A. Aguirre, K. K. Shung, Q. Zhou, M. Sanders, M. Brewer, and Q. Zhu, "Integrated optical coherence tomography, ultrasound and photoacoustic imaging for ovarian tissue characterization," Biomed. Opt. Express 2(9), 2551-2561 (2011).

Conference papers

1. **T. Wang,** Y. Yang, U. Alqasemi, P. Kumavor, X. Wang, M. Sanders, M. Brewer, and Q. Zhu, "Quantification of photoacoustic microscopy images for ovarian cancer detection," Proc. SPIE 8943, 894306 (2014).

2. H. Salehi, **T. Wang,** H. Li, P. Kumavor, and Q. Zhu, “Co-registered ultrasound and photoacoustic probe with a miniaturized light illumination scheme for in vivo ovarian cancer imaging,” OSA Biomed. Opt. (2014).
3. H. Salehi, P. Kumavor, U. Alqasemi, H. Li, **T. Wang,** and Q. Zhu, “High-throughput fiber-array transvaginal photoacoustic probe for in vivo ovarian cancer imaging,” Proc. SPIE 8943, 894335 (2014).
4. **T. Wang,** Y. Yang, X. Wang, M. Sanders, M. Brewer, and Q. Zhu, “Characterization of ovarian tissue using polarization-sensitive optical coherence tomography,” Proc. SPIE 8571, 857124 (2013).
5. **T. Wang,** Y. Yang, U. Alqasemi, P. D. Kumavor, M. Brewer, and Q. Zhu, “Photoacoustic microscopy for ovarian tissue characterization,” Proc. SPIE 8581, 85814M (2013).
6. Y. Yang, **T. Wang,** M. Brewer, and Q. Zhu, “Measurement of angle-resolved scattering property of ovarian tissue by use of OCT,” Proc. SPIE 8571, 85711Q (2013).
7. Y. Xu, S. Zanganeh, I. Mohammad, A. Aguirre, **T. Wang,** Y. Yang, L. Kuhn, M. B. Smith, Q. Zhu, “Target tumor hypoxia with 2-nitroimidazole-ICG dye conjugates,” Proc. SPIE 8578, 85781Z (2013).
8. **T. Wang,** P. D. Kumavor, and Q. Zhu, “Applying laser pulse stretching technique on photoacoustic imaging for efficiently delivering laser energy,” Proc. SPIE 8223, 822347 (2012).

9. Y. Yang, **T. Wang,** N. Biswal, X. Wang, M. Sanders, M. Brewer, and Q. Zhu, "Assessment of collagen changes in ovarian tissue by extracting optical scattering coefficient from OCT images," Proc. SPIE 8213, 82130C (2012).
10. Y. Yang, **T. Wang,** N. Biswal, P. Kumavor, X. Wang, M. Karimeddini, J. Vento, M. Sanders, M. Brewer, and Q. Zhu, "An intraoperative probe combining positron detection and OCT imaging for ovarian cancer detection and characterization," Proc. SPIE 8220, 82200E (2012).
11. Y. Yang, **T. Wang,** and Q. Zhu, "A novel prototype hybrid probe for in vivo ovary evaluation," BMES Annual Meeting (2011).
12. Y. Yang, N. C. Biswal, **T. Wang,** P. Kumavor, M. Karimeddini, M. Sanders, M. Brewer, and Q. Zhu, "A hybrid positron and OCT intraoperative probe for ovarian cancer detection and characterization," Proc. SPIE 7892, 78920Y (2011).
13. Y. Yang, X. Li, **T .Wang**, P. Kumavor, Q. Zhou, and Q. Zhu, "A combined photoacoustic, pulse echo ultrasound and optical coherence tomography endoscopy," Proc. SPIE 7899, 78994C (2011).
14. Y. L. Chen, Y. Yang, J. Ma, J. Yan, Y. Shou, **T. Wang**, A. Ramesh, J. Zhao, and Q. Zhu, "3D imaging of dental hard tissues with Fourier domain optical coherence tomography," (Invited paper) Proc. SPIE 7883, 78834O (2011).
15. Y. Yang, N. C. Biswal, P. Kumavor, **T. Wang,** M. Karimeddini, M. Sanders, M. Brewer, and Q. Zhu, "A miniature prototype hybrid intraoperative probe for ovarian cancer detection," OSA Biomed. BSuC7 (2010).